Spatial distribution and energy release of non-volcanic tremor at Parkfield, California

Nadine Staudenmaier[1], Benjamin Edwards[2], Thessa Tormann[1], J. Douglas Zechar[1] and Stefan Wiemer[1]

1. Swiss Seismological Service, ETH Zurich, Zurich, Switzerland.
2. Department of Earth, Ocean and Ecological Sciences, University of Liverpool, Liverpool, UK.

Corresponding author: Nadine Staudenmaier (nadine.staudenmaier@sed.ethz.ch)

Key Points:

- M_e is an ideal choice to describe energy release and characteristics of non-volcanic tremors
- Non-volcanic tremors in Parkfield release energy of the same order as M~1.5 earthquakes
- Spectral analysis strongly suggests that Parkfield's tremors are located in a 3D cloud-like cluster

Abstract

Non-volcanic tremors (NVTs) are observed in transition zones between freely slipping and locked sections of faults and normally occur below the seismogenic zone. Based on NVT recordings in the Parkfield region of the San Andreas Fault, we provide a novel approach to assess the energy release of these events and assign magnitudes (M_e) that are compatible with size estimates of small earthquakes in the same region. To assess the energy magnitude of a detected tremor, we refine the estimate of its duration and perform a spectral analysis that accounts for local attenuation.

For the 218 NVTs that we were able to process, we resolve M_e values in the range of -0.67 to 0.84. For events, which we could not process using the spectral analysis technique, we propose a statistical model to estimate M_e values using observable characteristics, such as peak amplitude, spectral velocity at the source corner frequency and duration. We furthermore provide seismic moment and moment magnitude estimates and calculate stress drops in a range of 3-10kPa.

As a result of our spectral analyses, we find strong indications regarding the on-going debate about potential NVT location hypotheses: the Parkfield NVTs have a higher probability to be located in the proposed three-dimensional cloud-like cluster than in any other suggested location distribution.

1. Introduction

Understanding stress accumulation and release along active fault zones is a fundamental challenge in seismological research. Over the last few decades, increasingly sensitive seismic networks enabled the discovery of additional fault slip phenomena, such as slow slip events, low and very low frequency earthquakes (Ghosh et al., 2015; Ito et al., 2007*)* and non-volcanic tremor (NVT) (Shelly et al., 2006; Shelly et al., 2007; Rogers and Dragert, 2003, Nadeau et al., 1995, Rubinstein et al., 2012). Much about these signals remains to be investigated, including their overall role in stress release and resulting effect on seismic hazard. In this study, we focus on NVT.

Since their discovery by Obara in 2002, NVTs have been documented at several tectonic plate boundaries around the world, both in subduction zones and near transform faults, extending below the seismogenic zone (Obara, 2002; Nadeau and Dolenc, 2005). NVT activity is

characterized by low amplitude seismic signals lasting a few minutes to several days with frequency content usually concentrated between 1 and 15Hz. Unlike earthquakes, tremor waveforms show emergent characteristics and usually do not contain any clear P- or S-arrivals. Their signals generally contain at least some short pulsating bursts of larger amplitude energy enclosed in lower amplitude activity (Zhang et al., 2010). Because of their deep location, NVTs allow us to investigate deep fault zone phenomena and may provide insights into the deep crust and its stress release processes.

The physics of tremor generation is not yet understood, but we know that tremor signals are different to earthquake signals in terms of duration and waveform. It is therefore not obvious how the size of such events should be characterized consistently. The size of an earthquake is usually described by a magnitude. There are numerous types of magnitude that use time or frequency domain analysis of observed waveforms.

Different types of magnitude scales have been previously applied to NVT signals. Because tremors last minutes to weeks and lack impulsive wave arrivals, using their duration to measure their energy release seems obvious. Along these lines, Ide et al. (2007) presented a scaling law for slow earthquake phenomena, including deep tremors at subduction zones. Those events are characterized by a stress drop of about 10kPa, two orders of magnitude smaller than earthquake stress drops. Ide et al. (2007) suggested that tremors arise from shear slip, just as regular earthquakes, but with longer durations and much less seismic energy radiated in the process. To estimate the released energy, they proposed that a tremor's seismic moment release is proportional to its duration.

Aguiar et al. (2009) also suggested a relation between tremor duration and seismic moment in Cascadia, showing that moment release could be inferred from joint GPS and seismic tremor monitoring. Cascadia has long been instrumented with both GPS and seismic networks, so it is an ideal setting to calibrate moment release during tremor events through time. The proportionality between duration and moment release is based on the observation that tremor episodes, which last 1–5 weeks and show cumulative tremor activity between 40 and 280 h, seem to be rather invariant in amplitude and frequency content, both between events and with

duration. Following this study, Wech et al. (2010) showed a correlation between the GPS-estimated moment release for each event and the duration of the recorded tremor. They estimated cumulative moment magnitudes M_w between 5-7 for tremor episodes in Cascadia.

Other studies suggest estimating NVT energy release by spectral waveform analysis. For example, Kao et al. (2005) quantified the energy release of tremor by comparing the frequency spectra of local earthquakes and episodic tremors in northern Cascadia. The spectra revealed that a tremor is similar to an M_L=1.5 earthquake in energy at low frequencies (up to 5 Hz). Kao et al. (2010) estimated seismic moments of deep NVT bursts in northern Cascadia based on the relationship between the seismic moment of a seismic source and the observed waveforms at individual stations. They defined an NVT burst as the maximum amplitudes at individual stations within ±5 s around the predicted arrivals of the S-wave, and they estimated M_w of about 1.0–1.7 for most tremor bursts. Fletcher and McGarr (2011) presented a similar analysis based on displacement spectra of high amplitude phases in two NVT signals in Parkfield. They showed that these phases with a defined duration of 30s in the tremor correspond to seismic moments around 3-10x10^{11} Nm or moment magnitudes M_w in the range of 1.6-1.9. Maeda and Obara (2009) introduced a method using envelope correlation (Obara et al. 2002) to estimate the radiated seismic energy of a tremor together with its source location from continuous seismic records. Their method combines the spatial distribution of tremor amplitude observed at a set of stations with the relative travel-time measurement for low-frequency tremors in western Shikoku. They obtained an energy radiation of the tremor per minute of 10^5 –10^6 J. Annoura et al. (2016) used this method to estimate the total energy of tremor activity in Nankai subduction zone during 2004–2015, and reported spatially varying tremor energy release. In 2014, Yabe and Ide investigated the spatial distribution of seismic energy rate of tectonic tremors in subduction zones (based on method of Maeda and Obara 2009). All of these studies related to estimating tremor energy release have a problem: they consider energy only from a limited bandwidth, usually frequencies between 2-10 Hz. While those frequency ranges typically contain the tremor's highest spectral amplitude, the resulting energy estimate must be considered a lower bound (Obara and Hirose, 2006). As argued by Maeda and Obara (2009), the total tremor energy should be the sum of contributions from all frequencies.

Not only is it difficult to estimate the energy release of NVTs, but signal complexity and the lack of clear P- and S-wave arrivals make it difficult to precisely locate NVTs. In particular, tremor depth is often poorly resolved. Several methods have been proposed to locate NVTs, including cross correlation time alignments of the similarly shaped energy envelopes of the tremors. This is done by converting station pair differential arrival times into individual arrival times at different stations (Obara, 2002; Nadeau and Dolenc, 2005; Nadeau and Guilhem, 2009). Another approach is to use station pair differential arrival times and find the location that minimizes the differences between observed and theoretical differential times (Suda et al., 2009) NVTs can also be located by searching for the location that maximizes tremor signal coherency among seismic stations (Wech and Creager, 2008). For all of these methods, the accuracy of the location is strongly influenced by the assumed velocity model (Zhang et al., 2010).

At subduction zones NVTs are assumed to be distributed on the plate interface below the seismogenic zone (Obara et al., 2002, Kao et al., 2005, Aguiar et al., 2009, Shelly et al., 2006, 2007, Ide et al., 2007, Brown et al., 2009, La Rocca et al., 2009). Along the San Andreas Fault (SAF), several methods to locate tremor have been applied, yielding different hypotheses regarding the spatial distribution of NVT. According to cross correlation (Nadeau and Guilhem, 2009), and re-assessed by a station-pair double-difference location method (Zhang et al., 2010), NVTs in Parkfield are observed at depths of 15-45 km, i.e., in the ductile lower crust around the Mohorovicic discontinuity, which is estimated to be 25 km in this part of California (McBride and Brown, 1986). NVTs occur along the SAF around Parkfield and form two clusters: the Monarch Peak cluster northwest of Parkfield and the Cholame cluster, which contains ~90% of the tremor activity and is located ~30km southeast of Parkfield (Figure 1). The Cholame NVTs seem to be located in a 3-dimensional cloud-like structure with a lateral extension of 15 km on either side of the fault and a depth extension from 10km down to 40 km (Nadeau and Guilhem, 2009; Zhang et al., 2010). Another suggestion for those NVTs is that they are all located on the fault plane close to Moho depth (Shelly, 2010). This high activity tremor cloud is situated below and beyond the southern extent of the recorded microseismicity along the SAF. Located in the area in which the SAF changes from creeping to fully locked behavior, those Cholame tremors can potentially provide new information about this transition zone and help to understand the governing processes in this unusual setting.

NVTs do not have a precise, universally accepted definition. This, coupled with the variety of methods for estimating NVT size and location, makes comparing the results of tremor studies difficult. Furthermore, moment magnitude is not an ideal solution because it can only be related to the energy released at low frequencies. Similar limitations are also found for other types of magnitudes: local magnitude only focuses on maximum amplitudes and duration magnitude neglects the amplitudes and purely considers the signal duration. None of these magnitude types seems suitable to fully address the complexity of an NVT signal. We overcome these limitations in this study by introducing energy magnitudes (M_e) for complete NVTs: M_e accounts for both amplitude and duration, and includes the full frequency bandwidth of the signal (Boatwright et al., 2002). But its determination is non-trivial, since the measurement of radiated seismic energy requires one to deconvolve attenuation and site effects. In this study, we present an analysis scheme to assess energy magnitudes for non-volcanic tremors in Parkfield. We show that the obtained values scale well with magnitudes of small local earthquakes. In addition, we analyze for the first time stress drops for Parkfield's NVTs and discuss parameters influencing their energy content. Finally, we derive a probabilistic ranking of different location hypotheses that have been suggested for the Parkfield observations.

2. Setting, Networks, and Data

The Parkfield section of the SAF has long been recognized as an ideal natural laboratory for studying crustal fault phenomena. Being the transition zone between the freely creeping fault section to the north and the fully locked Fort Tejon section to the south, the Parkfield segment has caught seismologists' attention by regularly producing M6 earthquakes about every 22 years. Within the framework of the Parkfield Earthquake Prediction Experiment (Bakun, 1985), dense networks of various instruments have been installed and tremendous data sets of high quality have been collected, making this area one of the most extensively monitored and best-studied fault sections on Earth.

The High Resolution Seismic Network (HRSN) is one element of this observatory. Operated by the Berkeley Seismological Laboratory, the HRSN is an array of geophone borehole instruments deployed in the Parkfield area, with the goal of monitoring microseismicity on the SAF. It contains 13 3-channel stations located on both sides of the SAF (Figure 1) at 63 to 345 m depth

(HRSN, 2014). While the noise level for borehole stations is generally much lower than for a surface network, there are still significant quality differences between the 13 stations. Upgrades of the instruments have been performed at different times over the last decade to improve noise sensitivity and enhance seismic signals.

Since 2001, the HRSN has recorded almost 3500 NVTs in the Cholame region south of Parkfield towards and beneath the adjacent locked section (HRSN, 2014). The average distance between the middle of the cloud and the HRSN stations is 40 km (Figure 1).

Closer to the tremor cloud, the Tremorscope stations complement the HRSN monitoring activity at Parkfield. Those stations are designed to provide additional refinement of origin locations for the observed NVT events in an up-to-date catalog (Nadeau and Guilhem, 2009 and Zhang et al., 2010). For this study, data have been obtained from the Tremorscope catalog (Nadeau and Guilhem, 2009), which distinguishes recorded NVTs of different quality: Quality A denotes well-recorded and well-located (via cross correlation) tremors, Quality B less well located, and Quality C tremors either could not be located or were superposed with earthquake signals. Each quality class contributes about one third to the total number of observed tremors. For this study we consider only Quality A NVTs recorded between mid 2003 to August 2011 in the Cholame region south of Parkfield. The location uncertainty for these events is ±3-4 km horizontally and ±5 km in depth. We note that some of the Quality A tremors have been relocated using a double difference technique (Zhang et al., 2010). The relative distribution of locations remains very similar, while the absolute location of the cloud is estimated 3 km shallower and about 4 km further north (Zhang et al., 2010). The durations reported for the Cholame events range from 3-22 minutes.

Based on the origin locations and duration estimates reported in the Tremorscope catalog, we obtained the original HRSN waveforms for all stations and all channels with a buffer window of 10 minutes before and after the reported tremor start and end times in the Tremorscope catalog. We processed all data (on all three channels) from the HRSN stations. We found that the quality of the tremor recordings varies significantly between stations due to site effects, local noise levels, and instrument upgrades happening at different times. For part of our analysis, we restrict our data set to the recordings of a selected reference station, which, due to very low noise and

undisturbed recording over long periods, recorded the maximum number of tremors (95% of all events passing analysis) among all stations. (The second best station only recorded about 60% of the total number of events.) Our reference station SMNB (or "Stockdale Mountain Borehole") is the third deepest in the network, with the sensor located at 282 m below the surface. The use of a reference station allows us to study the relative size differences between the tremor events, unbiased by site characteristics and amplification effects. It also allows us to test parameter sensitivity and thus quantify relative energy magnitude error estimates. We can also determine which parameters have the strongest influence on M_e. Beyond the detailed relative study based on the reference station data, we use the full set of recordings to check the variation of M_e estimates between the different stations.

3. Energy of NVTs

Calculating M_e, M_w, and stress drop for NVTs requires a complex processing scheme, which we detail in the following subsections. Here is a brief overview of the main steps:

- **Reassess duration:** The original durations (Nadeau and Guilhem, 2009) were based on a conservative detection algorithm designed to avoid falsely picking NVTs. We visually inspected the waveforms of detected tremor events and found that the algorithm yielded late start times and early end times. To estimate the full energy release of the events, we re-assess the NVT durations.
- **Analyze waveform spectra:** To estimate the energy from individual recordings, we apply a waveform analysis (Choy and Boatwright, 1995 and Boatwright et al., 2002) using a spectral fitting technique (Edwards et al., 2008) based on Brune's source model (Brune, 1970) and **frequency**-dependent attenuation (Raoof et al., 1999; Atkinson and Silva, 2000). We calculate the energy magnitude from the derived energy content.
- **Estimate moment magnitude and stress parameter:** To compare the M_e estimates with results from previous studies, we compute seismic moment (M_0) and moment magnitudes (M_w) for NVTs using a spectral fitting method based on Edwards et al. (2010). Furthermore, we provide stress parameter for those events.

3.1 Duration reassessment

The duration of each NVT was defined in Nadeau et al. (2009) as the length of the NVT's detection period. In other words, it is the length of time between the automatic detection's start and end time. Specifically, the start was defined as the point when the amplitude of the summary envelope first exceeds a detection threshold (SNR=3.0) and the end occurs when the envelope's amplitude falls below the detection threshold; only tremors with a duration greater than 3 minutes were reported. Examining these NVT detection durations from the Tremorscope catalog we frequently found that the noise level (measured 90 seconds before the NVT signal) was very high and that obtained NVT spectra could hardly be distinguished from the 'noise' (Figure 2, top right). As such, we could not analyze their spectra to estimate their energy magnitude. Nevertheless, visual inspection of the NVT waveforms showed that the tremor detection durations contain only a part of the complete tremor signal. This resulted in the measured noise window (90 seconds pre-signal) containing early parts of tremor, as illustrated in Figure 2.

To re-estimate tremor duration, we processed the waveforms for each reported tremor event, including ten minutes before the reported start and ten minutes after the reported end. We applied an acausal 6-pole Butterworth band-pass filter of 1-15 Hz to enhance the NVT signal (Figure 3a and b) and performed an SNR analysis over the reclaimed waveforms for all stations and channels. With a moving time window of 3 minutes, we assessed the continuous SNR of the squared amplitudes versus the channel-dependent pre-signal noise level. The selected time window of 3 minutes suppresses the influence of single spikes and micro-earthquake events while extracting the envelope of the waveform signal (Figure 3c and d).

To prevent bias from local influences and technical instrumentation issues, we stacked the SNRs from all stations and channels (indicated as grey lines in Figure 3e) and obtained an overall SNR envelope representing each event (black line in Figure 3e). We note that the close spacing between stations, compared to the network distance to the tremor source allowed us to use simple stacking. From processing several hours of background waveform data, selected throughout all years of recording and for different times of day, we found the noise level varies at most by a factor of 1.38. Waveform data containing earthquakes were excluded from the background noise analysis. Based on this analysis, we used an SNR of 1.5 to determine the beginning and the end of the re-defined durations (Figure 3e). As illustrated for one example (Figure 3g), spectrogram analysis was used to verify that the re-cut waveforms contain the full contribution of the tremor energy. We note that while the re-assessed start time of the NVT in Figure 3f seems early when

inspecting the time series at SMNB alone, the spectrogram analysis confirms the presence of NVT long before it is apparent in the time-series (approximately at 500 s), evident in the change in frequency content at about 400 s (and consistent with the SNR in Figure 3d).

The re-assessed tremor durations range from 4.33 to 22.70 minutes. The 'refined' durations are, on average, about six minutes longer than the original durations (see Figure 4). Shorter detection durations were more strongly affected by the re-assessment than longer ones. In six cases we observed a decrease in duration, which can be explained by pre-signal activity in the waveforms, interrupting the processing. Nevertheless, in only one case the re-assessed duration is significantly shorter than the catalog detection duration. This can be explained by two small earthquakes occurring shortly before and after the NVT, which strongly biases the start and end of the detection. In these rare cases our method fails, and we manually excluded from further analysis the one event that became significantly shorter.

3.2 Spectral waveform analysis

Spectral waveform analysis was applied to the re-cut tremor waveforms to estimate the energy from individual events (E_s**,** Choy and Boatwright, 1995 and Boatwright et al., 2002). The waveform signals and 90s noise windows were transformed from the time domain to frequency domain using the Fast Fourier Transform. When estimating E_s directly from the signal one risks including frequency content amplified by noise, especially concerning low quality recordings with a lower SNR. Therefore, we fit a model to the signal. This allows extrapolation of the NVTs frequency content beyond the limits of the noise-level and therefore provides a more accurate measure of energy.

To fit the obtained signal spectra, we followed the technique of spectral modelling described by Edwards et al. (2008), which uses Brune's earthquake source model (Brune, 1970). Our analysis implicitly treats the NVTs as earthquake sources – however, no distinction is made between a repeating source, or a slowly growing or migrating source. We limited our analysis to 0.5-50 Hz: while tremor signals typically have dominant signal in a range of 1-15 Hz, some contain clear signals up to 45 Hz. The spectra were corrected for frequency-dependent attenuation given by the frequency dependent quality factor:

$$Q(f) = Q_0 f^{\alpha} \quad (1)$$

The shear-wave attenuation in Southern California is on average well-described by $Q_0 = 180$ and $\alpha = 0.45$ (Raoof et al., 1999; Atkinson and Silva, 2000). From the frequency-dependent quality factor, we derived the whole path attenuation, t^*:

$$t^* = \frac{R}{\beta\, Q(f)} + \kappa_0 \quad (2)$$

with an average S-wave velocity of $\beta = 3500$ m/s and R as the hypocentral distance. High-frequency ground motions are also reduced by near-surface attenuation. This is described by the kappa-operator, κ_0 (Anderson and Hough, 1984). Regional estimates for κ_0 range from 0.02-0.04 s (Boore et al., 1992; Atkinson and Silva, 1997; Boore and Joyner, 1997), so a value of $\kappa_0 = 0.03$ was adopted.

We estimate the radiated NVT energy by integrating the velocity power spectrum corrected for the attenuation effect (Boatwright and Boore, 1982; Boatwright and Fletcher, 1987 and Boatwright et al., 2002):

$$E_s = 4\rho\beta R^{2\lambda} \left(\frac{1}{2F^s}\right)^2 2\pi \int_{f_1}^{f_2} (\dot{u}\,(f) e^{\pi t^* f})^2 df \quad (3)$$

with f_1=0.5 and f_2=50 as the lower and upper frequencies, $\dot{u}$ as spectral velocity, the average density $\rho = 2800$ kg m^{-3}, a radiation pattern coefficient $F^s = 0.55$ (Boore and Boatwright, 1984) and the geometrical decay exponent $\lambda = 1$. Finally, the derived energy content E_s was used to calculate the energy magnitude (Choy and Boatwright, 1995 and Boatwright et al., 2002):

$$\mathrm{M_e} = \frac{2}{3}(\log_{10} \mathrm{E_s} - 4.4) \quad (4)$$

3.3 Moment magnitude and Stress Parameter

To compare the obtained energy estimates to earlier studies we also computed seismic moment (M_0) and moment magnitudes (M_w) for NVTs using a spectral fitting method based on Edwards et al. (2010).

The seismic moment is calculated using the Brune (1970) scaling

315 $$M_0 = \frac{4\pi\beta^3\rho r_0}{FS}\,\mathrm{u}S(R) \qquad (5)$$

316 where F is the radiation coefficient (0.55 for SH waves), β is the near-source velocity (3.5 km/
317 s), S is the free-surface amplification (2.0), ρ is the average crustal density (2800 kg m^{-3}), r_0 is
318 the fault radius normalized to 1 km, u low-frequency level (plateau) of the displacement
319 spectrum and S(R) is the geometrical spreading function.
320
321 If a circular fault is assumed, the stress parameter $\Delta\sigma$ can be obtained from the seismic moment
322 M_0 and the source radius r_0 (Eshelby, 1957):

323 $$\Delta\sigma = \frac{7}{16}\frac{M_0}{r_0^3} \qquad (6)$$

324
325 The source radius is related to the corner frequency f_c by (Brune, 1971):

326 $$r_0 = 0.37\frac{\beta}{f_c} \qquad (7)$$

327 where β is the shear wave velocity near the source. By combining equations (6) and (7), we
328 obtain

329 $$\Delta\sigma = M_0\left(\frac{f_c}{0.4096\beta}\right)^3 \qquad (8)$$

330 where we will refer to $\Delta\sigma$ as stress drop. We note that these engineering-based, Brune-type stress
331 drop estimates are not necessarily equal to the true physical static stress drop of the earthquake
332 (Beresnev and Atkinson, 1997) but we use them in this study to describe the relative high
333 frequency content of NVTs.
334
335 **3.4 Results**
336 We processed 1068 'Quality A' tremors reported in the Tremorscope catalog. Since our duration
337 re-assessment requires 10 minutes before and after the original tremor start and end times.
338 We tested the influence of the picking algorithm on the signal duration: The arrival time
339 difference between stations is never larger than 3.2 seconds. The effect of this on a several
340 minute long signal is negligibly small in comparison to location uncertainty and attenuation
341 parameters (0.001-0.005 on magnitude).

If two tremors occur very close (less then 2min apart) in time our picking algorithm is not able to distinguish them properly. It is not able to find a clear end of the first or a start of the second one. (To make sure that we did not exclude a particular type of NVT we hand picked a subset and analyzed them). This reduces the data set to 704 events. Of those, 45% are contaminated by nuisance signals, such as small earthquakes (i.e. equivalent to falling into Tremorscope class C) and cannot be further processed. Temporary instrumental problems at the reference station reduce the remaining data set by another 5% to 371 tremors, which can be properly re-assessed for duration. To assure high quality data, we require a ratio between signal and noise in our spectral waveform analysis of at least two. This ratio results in a high goodness of fit (cumulative least-squares misfit smaller than 0.15) for 218 events. For those, our spectral waveform analysis is able to calculate energy magnitudes M_e, which range from -0.67 to 0.84 (calculated on reference station, Figure 5).

The corresponding moment magnitudes range from 1.29 to 1.89. This smaller span of magnitude range in comparison to the energy magnitude is explained by the difference in calculation of M_e and M_w. In general, M_w estimation neglects the high frequency content of the NVTs while M_e takes it into account. The high-quality Cholame NVTs show stress drops 3 to 9.7 kPa, which are only slightly lower than stress drops calculated by Ide et al. (2007) for deep tremors in subduction zones and of the same order as for very low frequency earthquakes (Ito and Obara, 2006). But they are significantly lower than the stress drops observed for earthquakes in this region (i.e. Allmann and Shearer, 2007). To obtain magnitude estimates for events not passing our spectral waveform analysis we provide scaling models in chapter 4.

Using the reference station, we thoroughly tested the sensitivity to parameters that may affect M_e, such as: the length of time windows (i.e. 1, 2 and 4 instead of 3 minutes for the NVT detection), minimum SNR for the duration re-assessment, SNR used in the spectral waveform analysis, and the influence of distance and lateral location uncertainty. We observe a contribution of about ± 0.03-0.08 units of magnitude for each variable, which is about 2-6 % in the magnitude range of interest. When we compare the M_e values obtained for the reference station with the M_e values we obtained by using all stations, we observe a variation of ±0.15 (or about 11%). To test the influence of the choice of the attenuation parameter, we conducted several tests. Using different Q_0 values between 160 and 240 (with α =0.45), a minor difference of about 0.04 in

magnitude was observed, which is of the same order as parameters discussed earlier. On the other hand, the choice of attenuation parameter α shows a strong effect on M_e, with up to ± 0.2 difference for α between 0.3 and 0.6. We verified the chosen value ($\alpha = 0.45$), as obtained by the earthquake based attenuation study of Raoof et al., (1999), by comparing the resulting total misfit between the spectral model and data over all NVTs for different values of α. A fixed Q_0 of 180 was used, while α was allowed to vary from 0.1 to 0.9. The best fit between modelled and observed NVT spectra was found for α = 0.42 (see Figure 6), very similar to the value found by Raoof et al. (1999) using earthquake recordings ($\alpha = 0.45$).

3.4.1 Consistency between earthquake and NVT magnitude estimates

We now explore how the energy magnitudes obtained for NVTs relate to the sizes of microseismic events. From the ANSS catalog, we selected 8 local earthquakes (locations indicated by violet stars in Figure 5), which are all located below 10 km. We processed these earthquake waveforms (recorded on the same reference station of the HRSN network) in exactly the same way as the NVTs with only one alteration – the time window for event onset picking: a 3 minute window would not be suitable for earthquakes, so a time window of 10s was applied.

Comparing the resulting spectra of an earthquake and an NVT with equal M_w of 1.6, shows a clear difference in corner frequency (Figure 7). While the earthquake spectra have a much larger content of higher frequencies than the NVT, both seismic events could be equally well fit by Brune's (1970) model, obtaining M_e=0.3 for the earthquake and M_e = -0.09 for the NVT. Figure 8 shows the scaling of the reference earthquakes' and NVTs' magnitudes, comparing M_e versus M_w estimates. We note that the M_w values, which we calculated for the earthquakes, are roughly equivalent to duration magnitudes (M_d) from the Northern California catalog, particularly for earthquakes above M_w=1.

The identical processing of both earthquake and tremor waveforms allows us to directly compare the energy release of the poorly understood tremors and that from the much-better-understood earthquakes. We find that the sizes of tremors that we derived via the energy magnitude estimation fall within the range of microseismic events in the Parkfield region, more specifically between moment magnitudes $1.3<M_w<1.8$.

4. Scaling relations for NVT M_e estimates

Due to their long-lasting signals, NVTs have often been quantified by duration alone (Kao et al., 2005; Aguiar et al., 2009 and Wech et al., 2010). In this study, we used the full tremor signal to estimate an energy magnitude for each event. In this section, we compare durations and energy magnitudes and find that magnitudes based only on duration are too simplistic. We investigate relationships between M_e and other NVT parameters to better understand which parameters influence NVT energy magnitudes. In particular, we present two statistical models that describe energy magnitudes in terms of other NVT parameters:

- Model 1 – based on easily obtainable tremor data, i.e. duration and amplitude and Parseval's theorem; and
- Model 2 – a physics-inspired model based on additional parameters that require Fourier transformation, i.e., spectral velocity at the source corner frequency.

These models could be used to estimate energy magnitudes for tremors without performing a full spectral waveform analysis; such an analysis is only possible for very high quality data.

4.1 Me versus duration and amplitude

Previous studies (Kao et al., 2005; Aguiar et al., 2009 and Wech et al., 2010) suggest a strong dependence of M_e on duration, but, as shown in Figure 9a, the Parkfield tremor data show only a weak correlation between duration and M_e (R^2=0.26). In other words, the energy of an NVT event is not determined only by its duration; the same is true for earthquakes (Aki and Richards, 1980). Moreover, because tremor durations vary so widely, maximum amplitude alone is not a sufficient measure of NVT energy. In Figure 9b, we show the relationship between maximum amplitude and energy magnitude (R^2=0.45).

As described by Eq. 4, energy magnitudes are based on the energy radiated by the source, E_s (for details see Eq. 3). E_s is related to the recorded energy E, which is, for a noise-free signal, either measured from the area under the velocity FAS (Fourier Amplitude Spectrum) squared, or equivalently from velocity (v), squared:

$$E = \int_0^\infty V(f)^2 df = \sum_0^N v(t)^2 dt \qquad (9)$$

Because the measured velocity signal is noisy, we estimate E using the modelled (i.e., noise-free) FAS, V_m. Then, from Parsevals theorem we have:

$$\int_0^\infty V_m(f)^2 df \cong \int_0^\infty V(f)^2 df = \sum_0^N v(t)^2 dt \cong c_3 \overline{v^2}\, T \quad (10)$$

Here, $\overline{v^2}$ is the mean velocity-squared of the whole signal trace, T is the signal duration and c_3 represents a proportionality constant. Fig. 9c shows how this expression correlates with M_e (R^2=0.71). An expression for M_e can then be defined as:

$$M_e = \frac{2}{3}(c_0 - c_1 \log_{10} R^2 + \log_{10}\left(\int_0^\infty V_m(f)^2 df\right) + c_{2a} R + c_{2b} R^2 - 4.4) \quad (11)$$

where c_0 is a modeling coefficient, c_1 is the geometrical spreading exponent ($A \sim R^{-c1}$), c_2 describes the energy lost due to attenuation (Q), and R is hypocentral distance. These terms are necessary to correct the observed signal for path and site effects.

By using Parseval's theorem (Eq. 10) Eq. 11 can be re-written:

$$M_e = \frac{2}{3}[c_0 - c_1 \log_{10} R^2 + c_{2a} R + c_{2b} R^2 + c_3 \log_{10}(\overline{v^2}\, T) - 4.4] \quad (12)$$

which forms the basis for Model 1:

$$M_e = a_0 + a_1 R + a_2 \log_{10} R^2 + a_3 R^2 + a_4 \log_{10}(\bar{v}^2 T) \quad (13)$$

We fit Model 1 to the 218 tremors described in Section 3.4 and obtained the following vector of coefficient estimates: $\boldsymbol{a}$ = {-3.4e1, -4.2e-1, 1.3e1, 2.0e-3, 5.0e-1}. For Model 1, the adjusted R^2 Model, which takes into account the number of predictors in the model, is 0.73, meaning that it explains 73% of the variation in M_e. Ten-fold cross-validation, which should be more conservative than fitting the entire dataset simultaneously (Maindonald and Braun, 2010), yields an adjusted R^2= 0.71.

462

463 **4.2 Me versus spectral velocity and corner frequency**

464 A tremor's physical characteristics—e.g., the size of the rupture patch, the amount of slip, and
465 the rupture velocity—should also determine how much energy it releases. These characteristics
466 are reflected by the spectral velocity at the corner frequency (related to a combination of slip and
467 the size of the rupture patch and the velocity of the rupture), and corner frequency itself (which is
468 inversely proportional to the rupture duration). We thus expect that those parameters play a role
469 in determining M_e. Indeed, we show in Figure 9d that energy magnitude is strongly correlated
470 with the logarithm of the spectral velocity observed at the corner frequency (R^2=0.90).

471

472 **4.3 A model for M_e of NVTs**

473 If we had perfect recordings that were not affected by attenuation and noise, Model 1 would fit
474 the energy magnitude data well. But we know our recordings are noisy and affected by
475 attenuation, so we therefore consider additional predictors. Because M_e is so strongly correlated
476 with spectral velocity at the source corner frequency, a model that includes this predictor is likely
477 to fit the data better than one that does not. Based on the findings in the previous sections and
478 following Stahel's (2004) principled approach to exploratory data analysis, we found a preferred
479 model, referred to as Model 2, which is based on spectral velocity at the source corner frequency,
480 squared mean-velocity, source corner frequency, and depth. Despite the fact that depth alone is
481 not very strongly correlated with energy magnitude, a model that includes depth is preferred
482 because it is physically reasonable and it improves the fit of the model. (Recall that in multiple
483 linear regression, just because the correlation between a predictor—here, depth—and the
484 response variable—magnitude—is not strong does not mean that including this predictor is a bad
485 idea; rather what is important is the correlation of the predictor and the residual of the starting
486 model). Model 2 is given by:

487

488 $$M_e = a_0 + a_1 \log_{10}\left(\overline{v_s}^2\right) + a_2 \log_{10}\left(V_{s,peak}\right) + a_3 \log_{10}(f_c) + a_4 \log_{10}(z) \qquad (14)$$

489

490 Where $\overline{v_S^2}$ is the average squared-velocity (time series) and $V_{s,peak}$ is the spectral velocity at the
491 source corner frequency, both corrected for Q and geometrical spreading (see Eq. 15):

$$\delta_{corr} = R\ \delta_{uncorr} \exp\left(\frac{\pi f R}{\beta Q(f)}\right) \qquad (15)$$

with δ_{uncorr} as parameter uncorrected for attenuation and δ_{corr} as attenuation-corrected parameter ($\overline{v_S^2}$ and $V_{s,peak}$), $\beta = 3.5\ km/s$, $f = f_c$ and $Q(f) = 180 f_c^{0.45}$, f_c is the source corner frequency, and z is depth (Figure 10a). Fitting Model 2 to the same data as used to fit Model 1, we obtained the following vector of coefficient estimates: $\boldsymbol{a} =$ {7.42142, 1.0225e-1, 1.23848e0, 2.8452e-1, 1.8829e-1}. This model yields an adjusted R^2=0.97. Ten-fold cross-validation yields an adjusted R^2=0.96. Other models with additional terms yield similar or even slightly higher values, but we prefer this model because it is easy to interpret and based on physical principles. Moreover, cross-validation suggests that we are not over-fitting: prediction intervals based on 10-fold cross-validation deliver the advertised coverage. And residual analysis (Fox, 2016) of Model 1 does not indicate any severe violations of the assumptions (i.e., normality, homoscedasticity, and independence of the errors) underlying multiple linear regression, suggesting that the model can be applied to other tremors.

As mentioned in subsection 3.4, our tremor data set contains many events that we cannot fully process. Some events have low SNR or are contaminated by nuisance signals, and we cannot reassess duration for some other events, which means that we cannot directly estimate M_e. Nevertheless, Model 2 allows to potentially increasing the number of NVTs with an estimate of energy magnitude. To test the performance of Model 2 (Equ. 14) we apply it to the same NVTs as in the high quality NVT data set from which it was derived. However, in this instance we assume that we were not able to reassess their durations. Squared mean-velocity is easily derived from the waveform. To obtain the spectral velocity at the source corner frequency it was necessary to assume artificial noise (noise level was fixed to intersect spectral velocity at 0.5 and 50 Hz and linearly interpolated between those two values) for this sub-signal to calculate an energy magnitude (see Section 3.1 and Figure 2) and fit it with Brune's model (Brune, 1970). In Figure 10b we compare the fully processed M_e results with the M_e values calculated from the basic parameters obtained from the sub-signal (with duration given by Tremorscope catalog and artificial noise level) using Model 2. We recover a very strong correlation of R^2=0.971.

5. Location probability based on flatness of acceleration plateau

Spectral waveform analysis provides us not only with energy magnitude estimates, but also with a tool to evaluate different hypotheses regarding the location and spatial distribution of Parkfield NVTs. There is an ongoing debate whether the NVTs are located:

- at their assigned locations in three dimensions (based on cross-correlation (Nadeau et al., 2009) and double-difference (Zhang et al., 2010), Figure 11a+d), or
- at their estimated lat/lon location but at Moho depth (Figure 11b+e), or
- on the fault plane, or
- on the fault plane at Moho depth (Shelly, 2010), or
- at a single point in space (Figure 11c+f).

The acceleration spectrum can be used to assess the quality of the attenuation model: for a good choice of the attenuation parameter Q(f), the spectral acceleration for well-located events flattens and forms a plateau at higher frequencies (Brune, 1970) when corrected for attenuation back to the source. The Parkfield area is well studied in many respects, including attenuation parameters (e.g. Raoof et al., 1999; Fletcher and McGarr, 2011; Boore et al., 1992; Atkinson and Silva, 1997; Boore and Joyner, 1997). In this study, we apply the attenuation model suggested by Raoof et al. (1999). Using the same, independently derived, attenuation model, we can test different tremor location hypotheses: the locations that lead to a spectral acceleration plateau at high frequencies are the most likely.

Processing the Parkfield tremor data set with different assumed locations shows the influence of source locations on the attenuation corrected FAS acceleration plateaus (Figure 11). With the 3D cloud-like location distribution based on cross correlation (Nadeau and Guilhem 2009), the acceleration plateaus are stable and flat for all tremor events (Figure 11e), and the corresponding velocity spectra show a regular behavior: a continuous sequence in energy magnitude as the spectral acceleration plateau increases (Figure 11a). When we force all tremors to Moho depth, keeping their latitude and longitude from the cross-correlation, we observe some convergence of the attenuation corrected acceleration spectra for higher frequencies (Figure 11f) and the velocity spectra are less well sorted in order of energy magnitude estimates (Figure 11b). When we force all tremors on to the fault plane, keeping their depths from the cross-correlation, we observe about the same convergence of the attenuation corrected acceleration spectra for higher

553 frequencies (Figure 11g) as for the locations fixed to the Moho and about a similar disorder in
554 the velocity spectra (Figure 11c). A clear divergence of the plateau and rather disarranged
555 acceleration spectra are observed if the NVT are assumed to originate all from the same spot in
556 the middle of the Cholame cloud (Figure 11d+h). By applying an over estimated α of 0.55 we
557 observe a clear decrease at higher frequencies in the acceleration spectra for all location
558 assumptions (Figure 11 i,j,k,l), which is caused by over correction. However, the original 3D
559 cloud locations based on cross correlation (Nadeau and Guilhem 2009) are still better (Figure
560 11i) than the other three cases (Figure 11j,k,l). Independent of the choice of alpha the relative
561 order of location goodness is preserved.
562 To formalize the location-quality comparison, for each NVT we analyze the flatness of the
563 attenuation-corrected acceleration spectrum between 25 and 49 Hz. With a perfect attenuation
564 model and the perfect location, the spectrum would be perfectly flat, and the ratio γ between
565 spectral acceleration estimate at 49 Hz, ω_{49Hz}, and spectral acceleration estimate at 25 Hz ω_{25Hz}
566 (Eq. 16), would be 1 (Figure 11a).
567

568 $$\gamma = \frac{\omega_{49Hz}}{\omega_{25Hz}} \qquad (16)$$

569

570 If the assigned location distance is overestimated, the attenuation-corrected acceleration
571 spectrum bends down due to over-corrected high frequencies, and γ becomes smaller than 1; and
572 vice versa for underestimated location distances (Figure 12a). To quantify these effects, we
573 analyze for each set of locations, γ for each tremor separately and calculate the mean ($\bar{\gamma}$) and the
574 standard deviation (σ_γ) of the γ estimates over all tremors. For an appropriate location
575 assignment (close to the truth), $\bar{\gamma}$ ≈1 and σ_γ will be small (Figure 12c). For a systematic shift of
576 the NVT locations away from (or closer towards) the recording station, a $\bar{\gamma}$ <1 ($\bar{\gamma}$ >1) and a
577 small σ_γ would be observed (Figure 12b, blue or purple). In cases of random mislocations, $\bar{\gamma}$
578 would again be close to 1, but σ_γ would become larger with increasingly worse locations (Figure
579 12b, all = black). Thus, neither $\bar{\gamma}$ nor the σ_γ alone can fully describe the probability of a location
580 set. A suitable measure is the absolute deviation of the $\bar{\gamma}$ from 1 (ideal case) plus the σ_γ.
581

In Figure 12d, we show a summary of numerous location hypotheses, assessed by this measure, showing their relative probability. Each hypothesis is represented by 1000 simulated catalogs or shown as a stem plot. For the single point hypothesis, we fix all NVTs to a random point in the Cholame cloud. For the shuffled hypothesis, we randomly shuffled true distances of tremors. We also tested the locations that result from a Gaussian perturbation (with σ = 1, 3.5, or 5 km) of the locations based on cross correlation (cc norm) (Nadeau and Guilhem, 2009). We also tried systematically shifting those cross-correlation locations 5 km closer to and 5 km further from the network. The Moho depth hypothesis results from shifting all NVTs to Moho depth (25km) while preserving their latitudes and longitudes. The sp dd represents station pair double-difference re-locations for NVTs up to beginning of 2009 (Zhang et al., 2010), also suggesting 3D cloud-like clustering. The on-fault plane hypothesis results from projecting the tremors onto the fault plane of SAF, preserving their distribution in depth. The 'Moho and on fault plane' hypothesis results from taking those locations that have been projected onto the fault and placing them at Moho depth (Shelly, 2010). Figure 12d supports the findings of Nadeau and Guilhem (2009) and Zhang et al., (2010) and shows that the Cholame NVTs are more likely to be distributed in a 3D cloud-like structure than in any other location assumption. This is even the case if we add a location uncertainty of +/- 5 km to the cross correlation locations (i.e., cc norm +/- 5km in Figure 12d).

Even though the cross-correlation locations yield flat FAS, there is still a slight deviation in the γ estimates from one. This could be caused by the applied attenuation model or by inaccurate locations. Assuming that the attenuation model is correct, this implies that the assigned locations are not accurate. To test how different they are from the true locations, we use a linear search to find, for each NVT, the distance $R_{optimized}$ that minimizes $|1-\gamma|$ (Figure 13a). In doing so, we find that the cross-correlation locations are too far from the network, i.e. on average, the whole Cholame cloud seems to be located about 1-1.5 km closer to the network (Figure 13b). To verify our findings and to test for the influence of α, we assessed differences between original and optimized distances for different α (Figure 13b histogram inset). We find that using α=0.45 based on Raoof et al, 1999 or α=0.42 obtained by spectral misfit analysis (Figure 6) has a negligible small effect on location (offset from cross correlation locations is1.44 km in average for α=0.45 and 1.27 km for α=0.42). However, perturbation α by 0.1 in either direction has a massive effect (Figure 13b inset).

6. Discussion

Adapting spectral waveform analysis typically used for earthquake signals to NVTs showed that it was necessary to refine the initial detection durations from the Tremorscope catalog (Nadeau and Guilhem, 2009). Ideally, such duration re-assessment should supplement future tremor detection algorithms following the initial, conservative detection (e.g., Nadeau and Guilhem, 2009). This two-step procedure would allow one to robustly detect NVTs while providing more precise start and end times (and therefore tremor durations). This will allow further studies to directly apply spectral waveform analysis using the reported durations and waveform characteristics.

As shown in this study, M_e is an appropriate quantification for the size of NVTs. Since M_e describes the full frequency content, it accounts for the differences between the NVTs in terms of radiated energy. In addition the derived M_w focuses on the low frequency content and the resulting 'collapsed' range for the same data set would suggest a far stronger similarity in terms of static slip characteristics than the dynamic faulting behavior between different NVT events.
With our processing scheme, which allows NVT signals and earthquakes alike to be processed, we could reveal that single NVTs in Cholame seem to release the same amount of energy as micro earthquakes with $1.3<M_w<1.9$. The observed consistency in scales between earthquake and NVT magnitudes allows for the first time to trust the absolute values of tremor magnitude with respect to magnitude scales that are commonly used for earthquakes.

We observed that the chosen attenuation parameter α has a major impact on the absolute energy magnitude values. Based on misfit analysis we determined α = 0.42 (Figure 6), which is very similar to the value found by Raoof et al. (1999) using earthquake recordings ($\alpha = 0.45$). This result suggests that the attenuation applied to the NVT signals is similar to that experienced during wave propagation from earthquakes originating much shallower than NVTs. Due to the formulation of Eqn. 1 with a single time used for each NVT event (source-site distance over average shear wave velocity) rather than the lag-time (e.g., as used in coda attenuation analysis) it also indicates that the recorded signal is dominated by an extended or repeating source signal, rather than dispersion of the wave field by scattering. We note that no significant change in the

relative energy distribution between events was observed even when fixing all NVT locations at the center of the Cholame tremor cloud.

How significant the influence of attenuation choices is, shows the comparison of our results with the study by Fletcher and McGarr (2011): They also applied spectral waveform analysis to two NVT events in Cholame but used different assumptions. However, they did not process the full several-minutes-long signal, but isolated a number of peaks, using ~30s long windows. Their study concentrated on the low frequency part, such that they chose to use frequency independent Q. For the individual peaks they obtained M_w values between 1.6 and 1.9 each. By implementing their attenuation assumption of $\alpha = 0$ (instead of 0.45), we could reproduce their results and obtain similar M_w for their data peaks. For M_w calculations, which focus only on low frequency content, attenuation does not have such a significant effect. Even by using $\alpha = 0.45$ the resulting M_w of 1.57 is very close to their value of 1.6 obtained with $\alpha = 0$. But for calculating M_e, which also includes high frequency content, attenuation becomes an important factor and adequate treatment necessary. Fletcher and McGarr also provide radiated energy estimates from their analysis, which could be directly translated to energy magnitudes (see Equation 4). Their obtained energy estimates are 100 times larger due to under estimation the influence of attenuation on higher frequencies. When applying an appropriate attenuation model (Raoof et al., 1999 and Atkinson and Silva, 2000) and allowing the whole frequency content as input, we obtain M_e = -0.3 for the largest data peak used by Fletcher and McGarr (2011) compared to their value of M_e=0.71. If we apply their attenuation assumption of $\alpha = 0$ to the whole NVT signal, instead of the peak, we observe an M_e= 1.4, instead of 0.03 ($\alpha = 0.45$).

The obtained engineering based Brune stress drop (Beresnev and Atkinson, 1997) is significantly lower for the NVTs than the stress drop observed for earthquakes in this region, but in the same range as observed by Fletcher and McGarr (2011). Similar stress drop estimates have been observed for very low frequency earthquakes in subduction zones (Ito and Obara, 2006, Ide et al., 2007). This low stress drop is in agreement with the observed low corner frequencies of about 4-12 Hz and indicates a slow slip process. Our findings consistently extrapolate the relation between seismic moment and the characteristic duration of slow slip and creep phenomena in the San Andreas Fault postulated by Ide et al., 2007.

675

676 We find that an NVT releases less energy than an earthquake with the same M_w (Figure 7). This
677 observed shift is in agreement with the lower corner frequency and smaller stress drop of NVTs
678 in comparison to earthquakes and indicates a slow slip process. We observed that the obtained
679 M_e values are approximately one unit in magnitude smaller than the corresponding M_w. By
680 comparing M_e and M_w it is important to understand the extent and physical nature of the
681 difference causing a general inequality between these two types of magnitudes. Energy
682 magnitude M_e is a complement to the moment magnitude M_w in describing the size of an
683 earthquake. M_e is obtained from the velocity spectra and represents the radiated seismic energy,
684 while M_w is derived from the low-frequency content of a displacement spectra and is therefore
685 more physically related to the static displacement of an event. M_w is normally larger than M_e as
686 observed in our resulting estimates and is only observed to be equal at a particular stress drop of
687 about 2-6 MPa (Choy and Boatwright, 1995). Earlier studies have suggested that there is a
688 potential relationship between earthquake stress drop and magnitude (e.g., Mayeda and
689 Malagnini (2009), de Lorenzo et al. (2010), Drouet et al. (2011), Edwards and Fäh 2013). In case
690 of the Cholame NVTs we did not observe a significant relation between their stress parameters
691 and the obtained energy magnitudes, however the magnitude range analyzed here was limited.

692

693 Contrary to previous studies (Kao et al., 2005; Aguiar et al., 2009 and Wech et al., 2010), our
694 analysis suggests that the energy release from individual NVT events is not well-described by
695 duration, amplitude, or their combination. This is likely caused by a variation of frequency
696 content and characteristics throughout the tremor signal itself. Longer tremors do not necessarily
697 release more energy: energy release is heterogeneously distributed throughout the event. This
698 suggests an alternating rupture behavior (patch size, slip, or velocity) throughout the NVT signal.

699

700 To better understand M_e, and to estimate it for NVTs which do not satisfy the high-quality
701 criteria of our processing scheme, we introduced a multiple linear regression model. The model
702 fits the data very well and could be used to enlarge tremor M_e data sets for future analysis. The
703 comparison of the model with the fully processed NVTs using high-quality data showed that it is
704 a reliable proxy for energy magnitude estimation.

705

706 The conducted spectral waveform analysis allows us to compare hypotheses of possible locations
707 for the Cholame NVTs. The proposed method of quantitatively testing for the flatness of the
708 attenuation corrected FAS acceleration plateaus is a novel approach to localize seismic events,
709 not only for NVTs but also earthquakes. If we have good a priori knowledge of the attenuation
710 processes in the study region of interest, this approach allows us to estimate the ideal distance of
711 each event from the network stations.
712
713 The results of this analysis provide strong evidence regarding the on-going discussion about
714 potential NVT location, finding that there is a much higher probability that NVTs in Parkfield
715 are clustered in the three-dimensional cloud, as has been proposed by cross-correlation (Nadeau
716 and Guilhem, 2009) and re-assessed with double-difference (Zhang et al., 2010). Our results
717 indicate that the locations may overestimate distance and the tremor cloud is, in reality, slightly
718 closer to the network. This observation is in good agreement with the independent re-localisation
719 approach via station pair double-difference relocation methods (Zhang et al., 2010), which
720 reports a shift of the cloud in depth (by 3.4 km) and towards the northwest (by 3.7 km) for
721 tremor events up to the beginning of 2009.
722

723 **7. Conclusions**

724 NVTs do not have a precise, universally accepted definition. This, coupled with the variety of
725 methods for estimating NVT size and location, makes comparing the results of tremor studies
726 difficult. Furthermore, moment magnitude is not an ideal solution because it only quantifies the
727 energy released at low frequencies, while local magnitudes only focusing on peak amplitudes
728 and duration magnitudes only on duration. We overcome these limitations in this study by
729 introducing energy magnitudes (M_e) for NVTs. The energy magnitude is an ideal choice for
730 assessing the energy release of NVTs: it takes into account the different characteristics of NVTs
731 more than moment magnitude, which focuses only on low frequencies. Furthermore, we found
732 that individual NVTs in Cholame seem to release the same energy amount as micro earthquakes
733 with $1.3<Mw<1.9$. Hence an NVT releases less energy than an earthquake with the same Mw,
734 due to their lower corner frequencies.

735 The Parkfield section of the SAF has long been recognized as an ideal natural laboratory for

736 studying crustal fault phenomena and the HRSN network with its borehole station provides an
737 ideal environment for studying NVTs. By adapting spectral waveform analysis to NVTs, we
738 found that it was necessary to refine the initial detection durations from the Tremorscope catalog
739 (Nadeau and Guilhem, 2009).

740 The attenuation model provided by Raoof et al., (1999) developed on earthquakes in this region
741 also applies to NVTs, located below the seismogenic zone. Our findings build on previous
742 studies (Kao et al., 2005; Aguiar et al., 2009 and Wech et al., 2010) that linked duration and
743 amplitude of NVT events by showing that the energy release from individual NVT events is not
744 well-described by duration, amplitude, or their combination alone.

745 To better understand M_e, and to potentially estimate it for NVTs which do not satisfy the high-
746 quality criteria of our processing scheme, we introduced a multiple linear regression model. This
747 model fits the data very well and might be used to enlarge tremor M_e data sets for future analysis.

748 Our method of testing for the flatness of the attenuation-corrected FAS acceleration indicates
749 that NVTs in Parkfield are clustered in a three-dimensional cloud, as has been proposed by cross-
750 correlation (Nadeau and Guilhem, 2009) and re-assessed with double-difference (Zhang et al.,
751 2010). Our results give evidence that the locations may overestimate distance and the tremor
752 cloud is, in reality, slightly closer to the network. This method represent a novel approach to
753 localize seismic events, not only NVTs but also earthquakes.

754 **Acknowledgments**

755 We want to thank Editor Martha Savage, Associate Editor Honn Kao, and two anonymous
756 reviewers for their valuable comments. This project is funded by the Swiss National Science
757 Foundation SNF: Project number 200021_149428. Data for this study come from the High
758 Resolution Seismic Network (HRSN) doi:10.7932/HRSN, operated by the UC Berkeley
759 Seismological Laboratory, which is archived at the Northern California Earthquake Data Center
760 (NCEDC), doi: 10.7932/NCEDC. The figures in this article were made using Generic Mapping
761 Tools (GMT) 5 software written by Wessel and Smith (1998).

762

763 **References**

764

765 Aguiar, A.C., Melbourne, T.I. and C.W. Scrivner (2009). Moment release rate of Cascadia
766 tremor constrained by GPS. J. Geophys. Res., 114, B00A05, doi:10.1029/2008JB005909
767
768 Aki, K. and Richards, P. (1980). Quantitative Seismology, W.H. Freeman, New York.
769
770 Allmann, B., and P. Shearer (2007), Spatial and temporal stress drop variations in small
771 earthquakes near Parkfield, California, J. Geophys. Res. 112, B04305,
772 doi:10.1029/2006JB004395.
773
774 Anderson, J. G., and S. E. Hough (1984). A model for the shape of the fourier amplitude
775 spectrum of acceleration at high-frequencies, Bull. Seismol. Soc. Am. 74, 1969–1993.
776
777 Annoura, S., Obara, K. and T. Maeda (2016). Total energy of deep low-frequency tremor in the
778 Nankai subduction zone, southwest, Geophys. Res. Lett.,doi: 10.1002/2016GL067780
779 Atkinson, G., and W. Silva (2000). Stochastic modeling of California ground motions, Bull.
780 Seism. Soc. Am. 90, 255–274.
781
782 Atkinson, G. M., and W. Silva (1997). An empirical study of earthquake source spectra for
783 California earthquakes, Bull. Seism. Soc. Am. 87, 97–113.
784
785 Bakun, W. H. and A. G. Lindh (1985). The Parkfield, California, earthquake prediction
786 experiment. Science 229, 619–-624
787
788 Beresnev, I. A., and G. M. Atkinson (1997). Modeling finite-fault radiation from the xn
789 spectrum, Bull. Seism. Soc. Am. 87, 67–84.
790
791 Boatwright, J., and D. M. Boore (1982). Analysis of the ground accelerations radiated by the
792 1980 Livermore Valley earthquakes for directivity and dynamic source characteristics, Bull.
793 Seism. Soc. Am. 72, 1843–1865.
794
795 Boatwright, J., and J. B. Fletcher (1987). The partition of radiated energy between P and S

waves, Bull. Seism. Soc. Am. 77, 361–376.

Boatwright, J., Choy, G.L., and C.S. Seekins (2002). Regional Estimates of Radiated Seismic Energy. Bull. Seism. Soc. Am. 92, 1241-1255.

Boore, D.M. and J. Boatwright (1984). Average body-wave radiation coefficients, Bull. seism. Soc. Am., 74, 1615–1621.

Boore, D.M. and W. B. Joyner (1997). Site amplifications for generic rock sites, Bull. seism. Soc. Am., 87, 327–341.

Boore, D., Joyner, W.B. and L. Wennerberg (1992). Fitting the stochastic ω−2 source model to observed response spectra in western North America: trade-offs between σ and κ, Bull. seism. Soc. Am., 82, 1956– 1963.

Brown, J. R., G. C. Beroza, S. Ide, K. Ohta, D. R. Shelly, S. Y. Schwartz,W. Rabbel, M. Thorwart, and H. Kao (2009), Deep low-frequency earthquakes in tremor localize to the plate interface in multiple subduction zones, Geophys. Res. Lett., 36, L19306, doi:10.1029/2009GL040027.

Brune, J, (1971), Correction: tectonic stress and spectra of seismic shear waves from earthquakes, J. geophys. Res., 76, 5002.

Brune, J. (1970), Tectonic stress and spectra of seismic shear waves from earthquakes, J. Geophys. Res., 75, 4997 – 5009.

Choy, G. L., and J. Boatwright (1995). Global patterns of radiated seismic energy and apparent stress, J. Geophys. Res. 100, 18,205–18,228.

de Lorenzo, S., A. Zollo, and G. Zito (2010). Source, attenuation, and site parameters of the 1997 Umbria-Marche seismic sequence from the

827

828 Drouet, S., M.-P. Bouin, and F. Cotton (2011). New moment magnitude scale, evidence of stress
829 drop magnitude scaling and stochastic ground motion model for the French West Indies,
830 Geophys. J. Int. 187, 1625–1644.

831

832 Edwards, B., and D. Fäh (2013). A stochastic ground-motion model for Switzerland, Bull. seism.
833 Soc. Am., 103(1), 78–98.

834

835 Edwards, B., B. Allmann, D. Fäh and J. Clinton (2010). Automatic Computation of Moment
836 Magnitudes for Small Earthquakes and the Scaling of Local to Moment Magnitude, Geophysical
837 Journal International 183, 407-420, doi: 10.1111/j.1365-246X.2010.04743.x.

838

839 Edwards, B., Rietbrock, A., Bommer, J.J. and B. Baptie (2008). The acquisition of source, path
840 and site effects from micro-earthquake recordings using Q tomography: application to the UK,
841 Bull. seism. Soc. Am., 98, 1915–1935.

842

843 Eshelby, J, (1957). The determination of the elastic field of an ellipsoidal inclusion, and related
844 problems, Proc. R. S. A, 241(1226), 376–396.

845

846 Fletcher, J. B., and A. McGarr (2011). Moments, magnitudes, and radiated energies of non-
847 volcanic tremor near Cholame, CA, from ground motion spectra at UPSAR. J. Geophys. Res. 38,
848 L16314, doi:10.1029/2011GL048636.

849

850 Fox, J. (2016), Applied Regression Analysis and Generalized Linear Models, Sage: Los Angeles,
851 792 pp.

852

853 Ghosh, A., E. Huesca-Pérez, E. E. Brodsky, and Y. Ito (2015), Very low frequency earthquakes
854 in Cascadia migrate with tremor, Geophys. Res. Lett., 42, doi:10.1002/2015GL063286

855

856 Hirose, H., and K. Obara (2006), Short-term slow slip and correlated tremor episodes in the
857 Tokai region, central Japan, Geophys. Res. Lett., 33, L17311, doi:10.1029/2006GL026579.

HRSN (2014), High Resolution Seismic Network. UC Berkeley Seismological Laboratory. Dataset. doi:10.7932/HRSN.

Ide, S., G. C. Beroza,, D. R. Shelly, and T. Uchide (2007), A scaling law for slow earthquakes, Nature, 447, 76-79, doi:10.1038/nature05780

Ito, Y., K. Obara, K. Shiomi, S. Sekine, and H. Hirose (2007), Slow earthquakes coincident with episodic tremors and slow slip events, Science, 315, 503-506, doi:10.1126/science.1134454

Ito, Y., and K. Obara (2006), Very low frequency earthquakes within accretionary prisms are very low stress-drop earthquakes, Geophys. Res. Lett., 33, L09302, doi:10.1029/2006GL025883.

Kao, H., K. Wang, K., Dragert, H., Kao, J. Y., and G. Rogers (2010), Estimating seismic moment magnitude (Mw) of tremor bursts in northern Cascadia: Implications for the "seismic efficiency" of episodic tremor and slip, Geophys. Res. Lett. 37, L19306, doi:10.1029/2010GL044927

Kao, H., S. J. Shan, H. Dragert, G. Rogers, J. F. Cassidy, and K. Ramachandran (2005), A wide depth distribution of seismic tremors along the northern Cascadia margin, Nature, 436, 841–844, doi:10.1038/nature03903.

La Rocca, M., K. C. Creager, D. Galluzzo, S. D. Malone, J. E. Vidale, J. R. Sweet, and A. G. Wech (2009), Cascadia tremor located near plate interface constrained by S minus P wave times, Science, 323, 620–623, doi:10.1126/science.1167112.

Maeda, T., and K. Obara (2009), Spatiotemporal distribution of seismic energy radiation from low-frequency tremor in western Shikoku, Japan, J. Geophys. Res., 114, B00A09, doi:10.1029/2008JB006043.

Maindonald J., and W. J. Braun (2010), Data Analysis and Graphics Using R:

An Example-Based Approach. 3rd Edition. Part of Cambridge Series in Statistical and Probabilistic Mathematics. Cambrigde, ISBN: 9780521762939

Mayeda, K., and L. Malagnini (2009). Apparent stress and corner frequency variations in the 1999 Taiwan (Chi-Chi) sequence: Evidence for a stepwise increase at M-w similar to 5.5, Geophys. Res. Lett. 36, 5 pp.

McBride, J. H., and L. D. Brown (1986), Reanalysis of the COCORP deep seismic reflection profile across the San Andreas Fault, Parkfield, California, Bull. Seismol. Soc. Am., 76, 1668–1688.

Nadeau, R.M., and D. Dolenc (2005). Nonvolcanic tremors deep beneath the San Andreas Fault: Science, v. 307.

Nadeau, R.M., and A. Guilhem (2009). Nonvolcanic Tremor Evolution and the San Simeon and Parkfield, California, Earthquakes: Science, v. 325.

Nadeau, R., Foxall, W., and T. V. McEvilly (1995). Clustering and periodic recurrence of microearthquakes on the San Andreas fault: Science, v. 267.

Obara, K, (2002). Nonvolcanic deep tremor associated with subduction in southwest Japan. Science 296, 1679–168.

Raoof, M., Herrmann, R.B., and L. Malagnini (1999). Attenuation and excitation of three component ground motion in southern California, Bull. seism. Soc. Am., 89, 888–902.

Rogers, G., and H. Dragert (2003). Episodic tremor and slip on the Cascadia subduction zone: the chatter of silent slip. Science 300, 1942–1943.

Rubinstein, J.L., Ellsworth, W.L., Chen, K.H., and N. Uchida (2012). Fixed recurrence and slip models better predict earthquake behavior than the time- and slip-predictable models: 1. Repeating earthquakes: J. Geophys. Res., v. 117.

Shelly, D. R. (2010), Migrating tremor illuminates deformation beneath the seismogenic San Andreas fault, Nature, 463, 648–652, doi:10.1038/ nature08755.

Shelly, D. R., G. C. Beroza, and S. Ide (2007), Non-volcanic tremor and low-frequency earthquake swarms, Nature, 446, 305– 307, doi:10.1038/ nature05666.

Shelly, D.R., Beroza, G.C., Ide, S., and S. Nakamula (2006). Low-frequency earthquakes in Shikoku, Japan, and their relationship to episodic tremor and slip: Nature, v. 442.

Stahel, W. A. (2003). Purposes and strategies in regression analysis.Journal of Statistical Planning and Inference 122 175–186.

Suda, N., R. Nakata, and T. Kusumi (2009), An automatic monitoring system for nonvolcanic tremors in southwest Japan, J. Geophys. Res., 114,B00A10, doi:10.1029/2008JB006060

Wech, A. G., Creager, K. C., Houston, H., and J. H. Vidale (2010). An earthquake- like magnitude- frequency distribution of slow slip in northern Cascadia. Geophys. Res. Lett., 37, L22310, doi:10.1029/2010GL044881

Wech, A. G., and K. C. Creager (2008), Automated detection and location of Cascadia tremor, Geophys. Res. Lett., 35, L20302, doi:10.1029/ 2008GL035458.

Yabe, S., and S. Ide (2014), Spatial distribution of seismic energy rate of tectonic tremors in subduction zones, J. Geophys. Res., 119, 8171-8185 doi:10.1002/2014JB011383.

Zhang, H., Nadeau, R. H., and M. N. Toksoz (2010). Geophys. Locating nonvolcanic tremors beneath the San Andreas Fault using a station-pair doubledifference location method. Geophys. Res. Lett., 37, L13304, doi:10.1029/2010GL043577

949 **Figure 1:** (Top) aerial view of the HRSN network and location distribution of processed high
950 quality NVTs in the Parkfield region of the SAF. Circle sizes and colors scale with duration;
951 triangles: locations of the HRSN stations, with the reference station SMNB marked in red; black
952 dots: detected but not processed tremor events. Shown waveforms are normalized in amplitude
953 and time. (Bottom) cross-section along the SAF indicating the different tectonic behavior of the
954 fault zone going from locked in the south to creeping in the north. Grey dots: local earthquakes
955 M>=1.3 (NCSN catalog from the Northern California Earthquake Data Center, 1985-2013),
956 yellow star: hypocentre of the 2004 M6 event.

957

958 **Figure 2:** Comparison of spectra of NVT with Tremorscope start time ID 20091108061620.00
959 with detection duration (top right) and with re-assessed duration (top left). By re-assessing the
960 duration a significantly improved distinction between NVT signal (black line in spectra) and
961 background noise (red line in spectra) was obtained. bottom: NVT time series indicating the
962 reported start and end times (yellow box). The re-assessed duration is indicated by the pink box.

963

964 **Figure 3:** Processing scheme from raw waveform to re-defined duration: a) unfiltered waveform
965 of NVT with Tremorscope start time ID 20091108061620.00 recorded on station SMNB vertical
966 channel; b) de-trended and band-pass filtered waveform between 1 and 15 Hz (same channel); c)
967 squared amplitudes of filtered velocity waveform (same channel); d) waveform envelope using a
968 3 minute window (same channel); e) stack of all waveform envelopes over all channels and all
969 stations, orange: original Tremorscope start and end-time of the NVT, violet: re-assessed start
970 and end-time of the NVT (cut-off level of 1.5); f) tremor waveform with original and new start
971 and end-times in orange and violet, respectively; g) spectrogram analysis of the NVT (station
972 SMNB vertical channel) overlaid with the stacked SNR (from panel e).

973 **Figure 4:** Comparison of detection durations based on the Tremoscope catalog (Nadeau and
974 Guilhem, 2009) and re-assessed duration based on the SNR analysis for the 219 events that pass
975 the high quality criteria (for details see text sections 3.1 and 3.2) of our duration-re-assessment
976 and spectral waveform analysis

977

978 **Figure 5:** distribution of energy magnitudes in the fault setting of SAF (same setting as in Figure
979 2). Circle sizes and colors scale with M_e; pink stars represent locations of selected earthquakes
980 used for magnitude comparison.

981

982 **Figure 6:** Spectral misfit of data and model at different choices of α- parameter for Q_0 fixed at
983 180. The smallest misfit is observed at $\alpha = 0.42$.

984

985 **Figure 7:** Differences between NVT (left) and earthquake (right) spectra (top) and waveforms
986 (bottom) both with M_w = 1.6; processed data (black), noise (red), and fit (blue), corner frequency
987 (green vertical line), frequency range (grey vertical line). The NVT event has a corner frequency
988 of 6.7 Hz and duration of about 10 minutes; the earthquake has a similar energy content as the
989 NVT, a corner frequency of about 15.7 Hz, and duration of about 10 seconds.

990

991 **Figure 8:** Moment magnitudes and energy magnitudes of a selection of earthquakes (violet stars)
992 and Cholame NVTs (blue dots) around Parkfield. Noted in black are type and magnitude
993 estimates for those earthquakes provided by the ANSS (NC) catalog.
994

995 **Figure 9:** Scaling relationships: a) M_e vs duration T; b) M_e vs. maximum amplitude (velocity)
996 vmax; c) M_e vs depth z ; d) M_e vs. attenuation-corrected peak spectral velocity at corner
997 frequency and e) M_e vs. $\log_{10}$(duration(T) *mean-velocity^2) representing Model 1

998

999 **Figure 10:** a) Model 2: processed M_e vs modelled M_e: Comparing energy magnitudes obtained
1000 by spectral waveform analysis (processed) and magnitudes estimated by model (modelled) b)
1001 processed M_e vs calculated (Eq. 14) M_e from original parameters obtained from the sub-signal
1002 based on duration given by the Tremoscope catalog.
1003

1004 **Figure 11:** Attenuation corrected velocity spectra (left), acceleration spectra with optimal
1005 attenuation α =0.45 (middle) and acceleration spectra with over estimated attenuation α =0.55
1006 (right) for different location hypotheses: (a,e,i) cross correlation locations, (b,f,j) located at

Moho, (c,g,k) located on fault, (d,h,l) all NVTs located at a single point in the middle of the Cholame cloud. Black arrows (in i and j) are illustrating effect of α on plateau.

Figure 12: a-c) Illustration how over- and underestimation of NVT location distances, or the combination of both, affect the acceleration spectra plateaus and the mean and standard deviations of high frequency FAS acceleration γ estimates between 25 and 49 Hz. Green: true location, blue: overestimated distance, magenta: underestimated distance, d) Location probabilities of different location hypotheses for the Cholame NVT data: increasing values of the absolute deviation of the $\bar{\gamma}$ from 1 (ideal case) plus the σ_γ correspond to less consistency between location/distance set and acceleration data (for details see text).

Figure 13: Re-assessing NVT locations in terms of their distance from the network. a) Each line shows, for a single NVT, the linear search for the most accurate distance $R_{optimized}$ (at y=0). b) Comparing the original distance to the network (R) with optimized distance ($R_{optimized}$). Inset: differences between original and optimized distances for different α: red histogram: under estimated attenuation; orange histogram: over estimated attenuation; light and dark blue histograms for appropriate attenuation models with α= 0.45 and 0.42: on average, original cross-correlation NVT distances are 1-1.5 km further from the network.

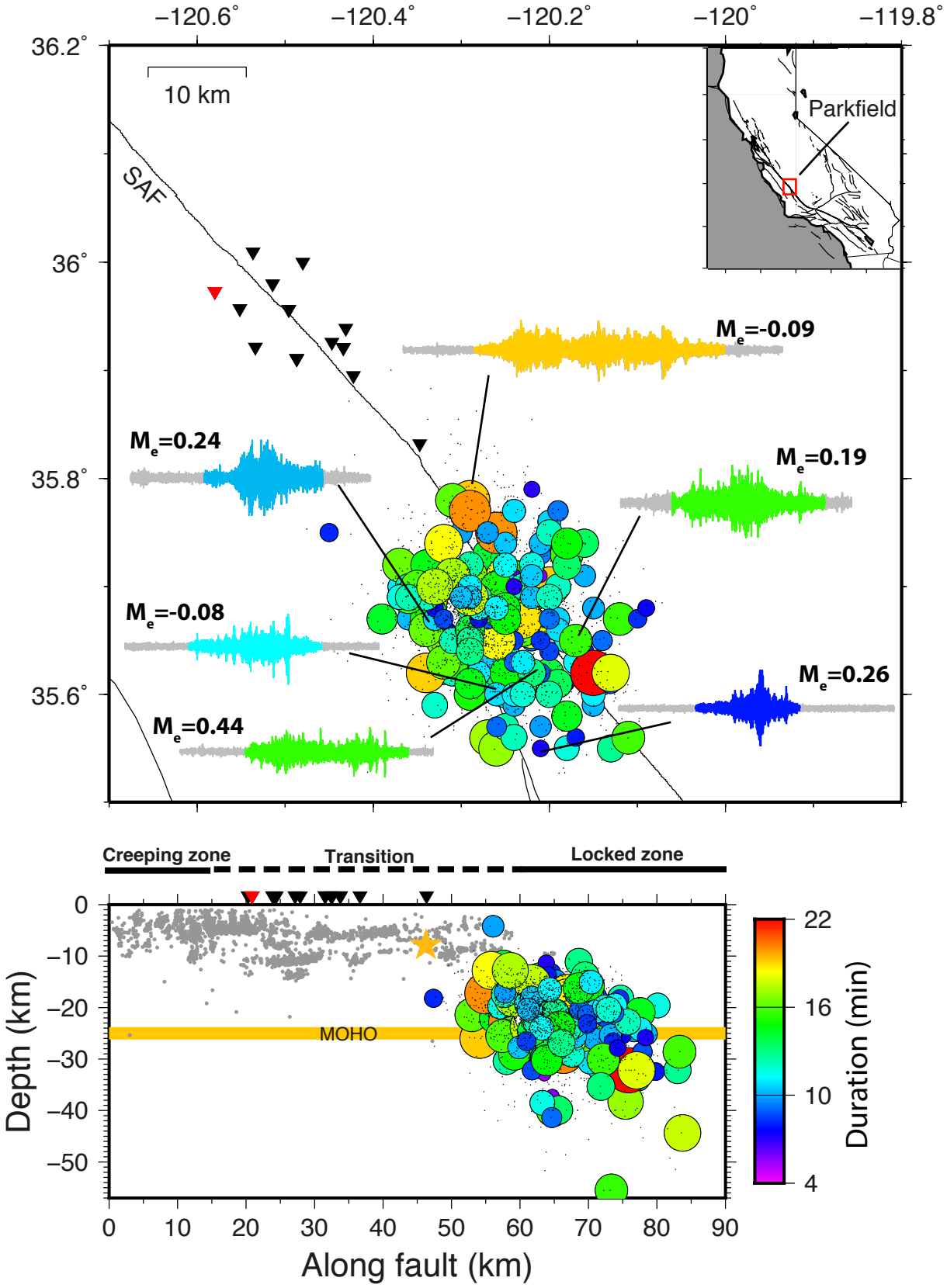
−120.6°
−120.4°
−120.2°
−120°
−119.8°
36.2°
36°
35.8°
35.6°
10 km
SAF
Parkfield
Me=-0.09
Me=0.24
Me=0.19
Me=-0.08
Me=0.26
Me=0.44
Creeping zone
Transition
Locked zone
MOHO
Depth (km)
0
−10
−20
−30
−40
−50
0
10
20
30
40
50
60
70
80
90
Along fault (km)
22
16
10
4
Duration (min)

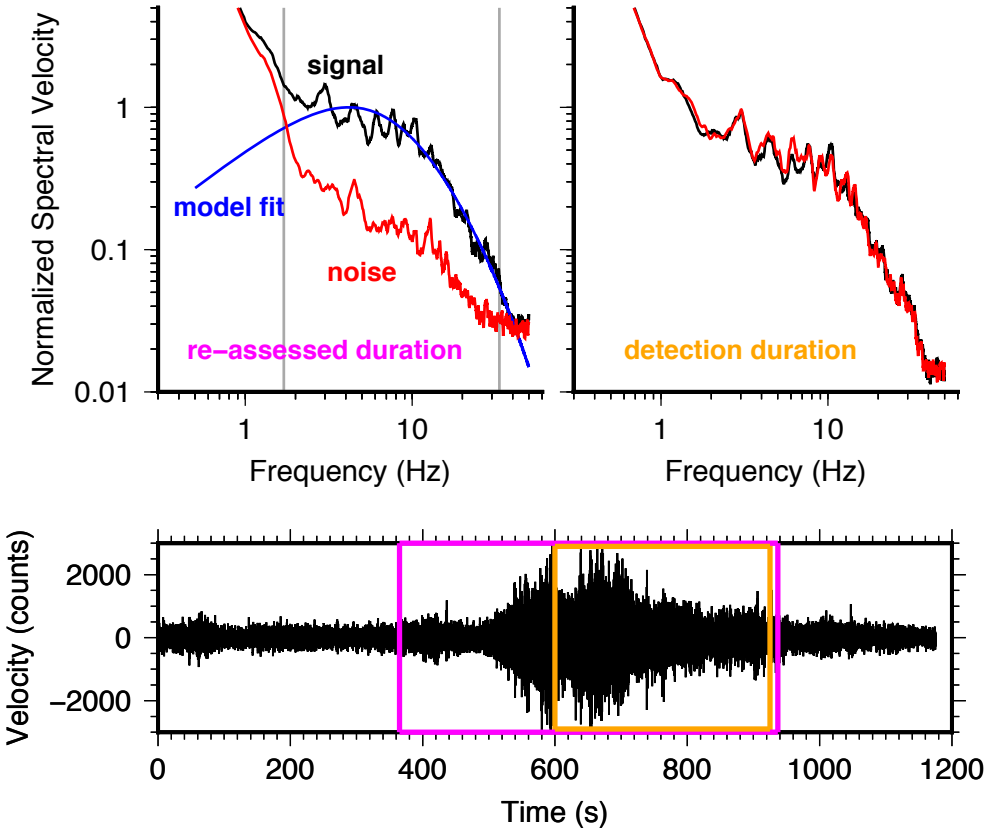
Normalized Spectral Velocity
1
0.1
0.01
signal
model fit
noise
re–assessed duration
detection duration
1
10
Frequency (Hz)
1
10
Frequency (Hz)
Velocity (counts)
2000
0
–2000
0
200
400
600
800
1000
1200
Time (s)

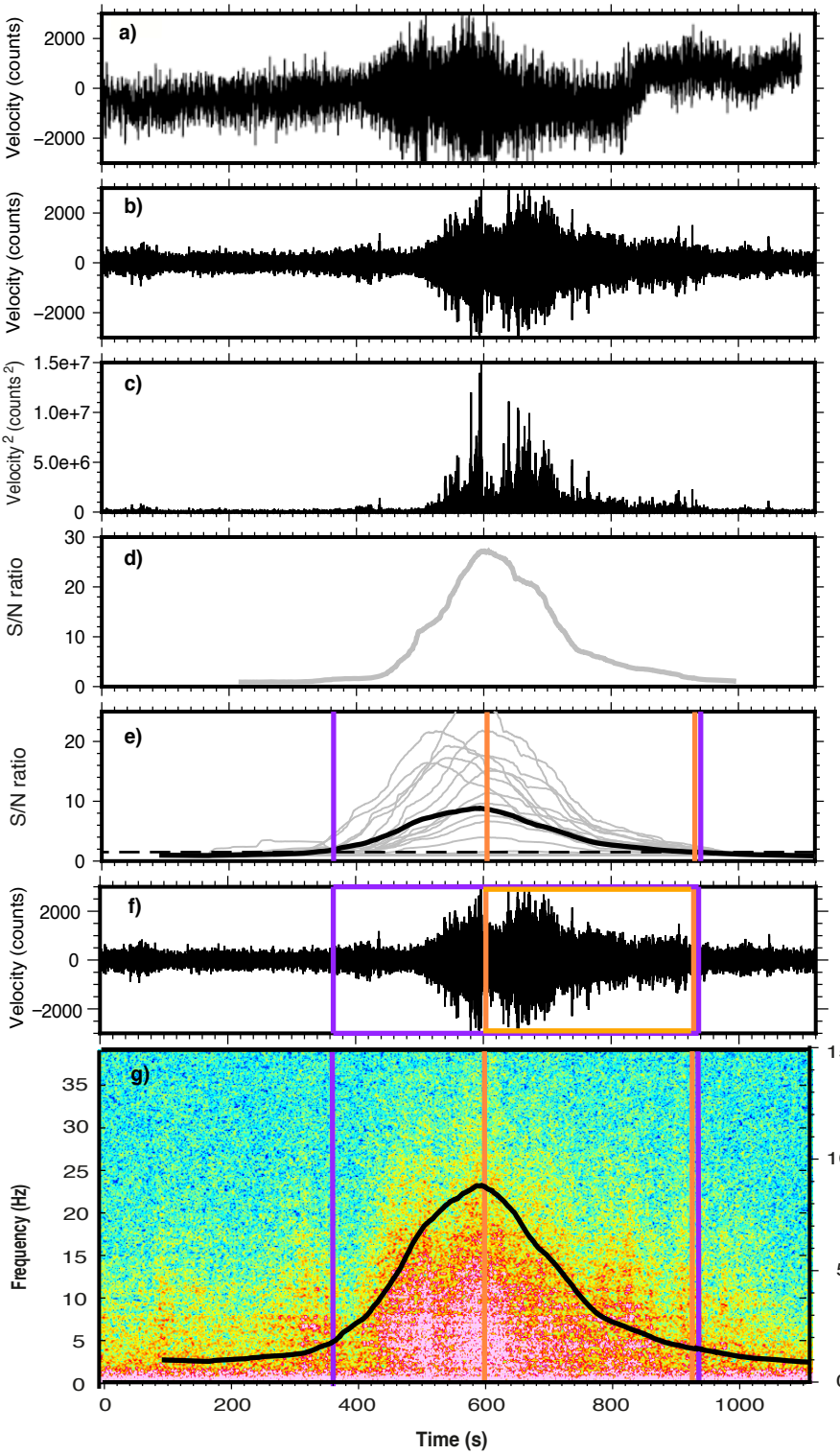
a)
b)
c)
d)
e)
f)
g)
Velocity (counts)
Velocity^2 (counts^2)
S/N ratio
Frequency (Hz)
Time (s)
2000
0
−2000
1.5e+7
1.0e+7
5.0e+6
30
20
10
15
5
35
25
200
400
600
800
1000

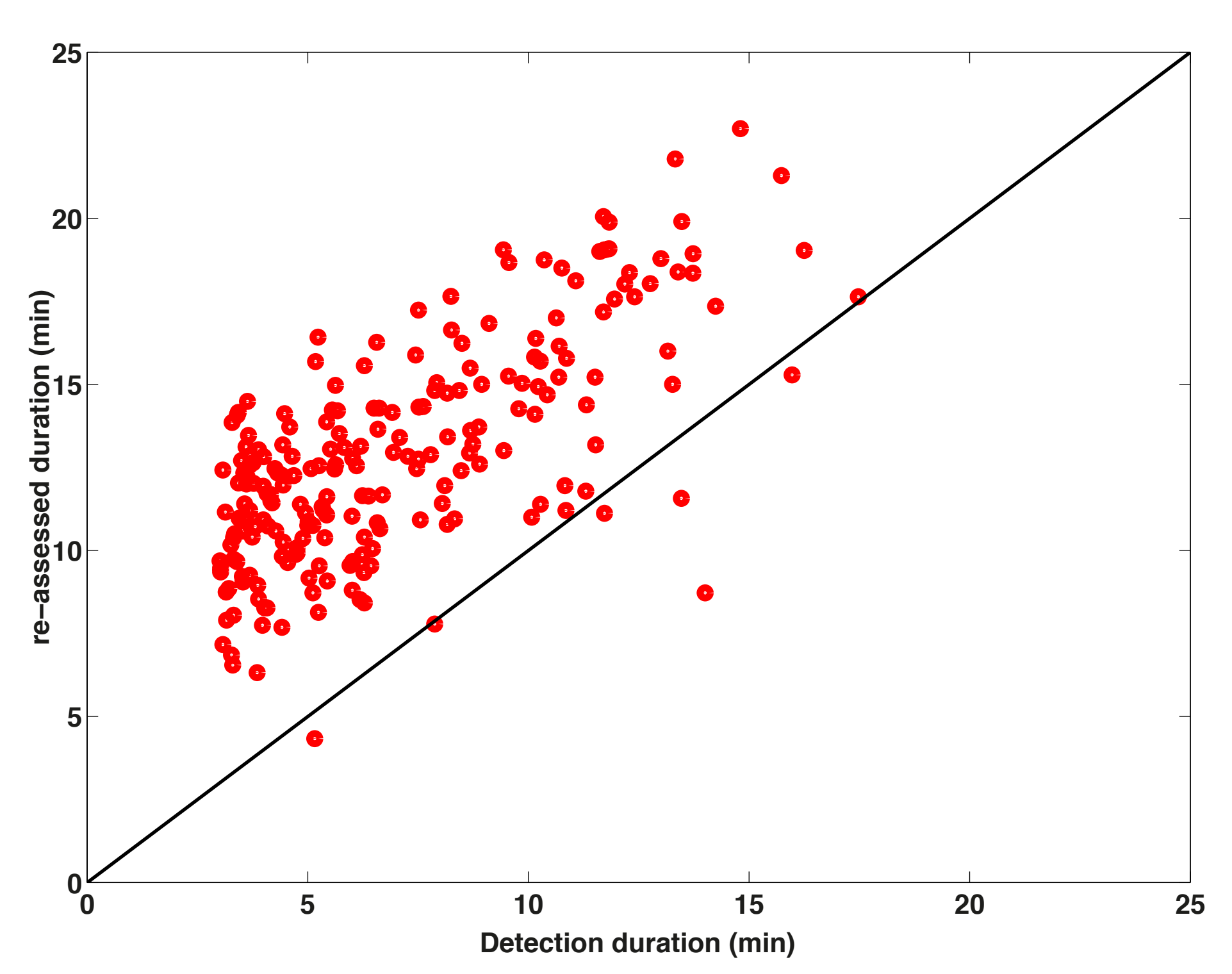
25
20
15
10
5
0
re–assessed duration (min)
0
5
10
15
20
25
Detection duration (min)

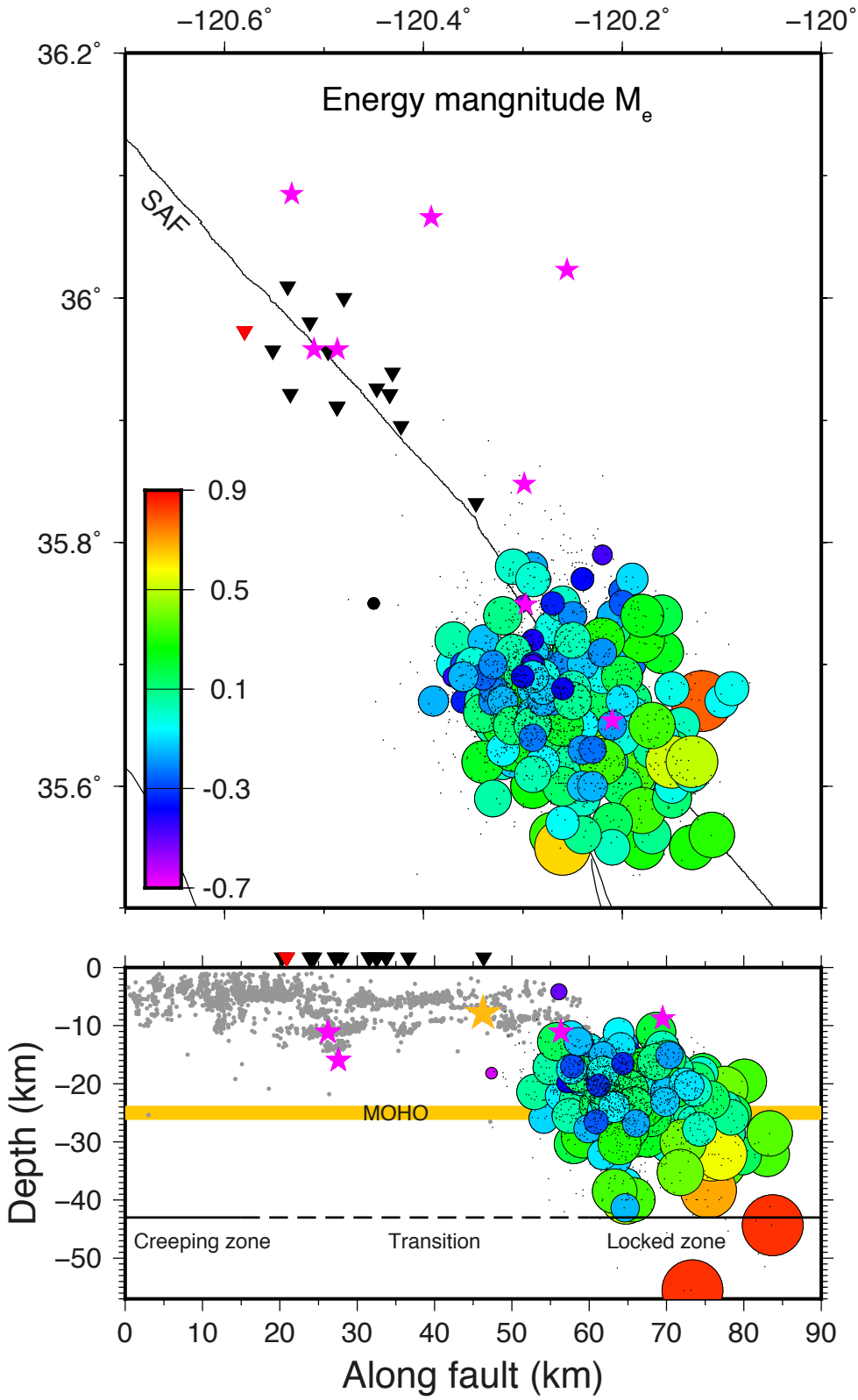
−120.6˚
−120.4˚
−120.2˚
−120˚
36.2˚
36˚
35.8˚
35.6˚
Energy mangnitude M_e
SAF
0.9
0.5
0.1
-0.3
-0.7
0
−10
−20
−30
−40
−50
Depth (km)
MOHO
Creeping zone
Transition
Locked zone
0
10
20
30
40
50
60
70
80
90
Along fault (km)

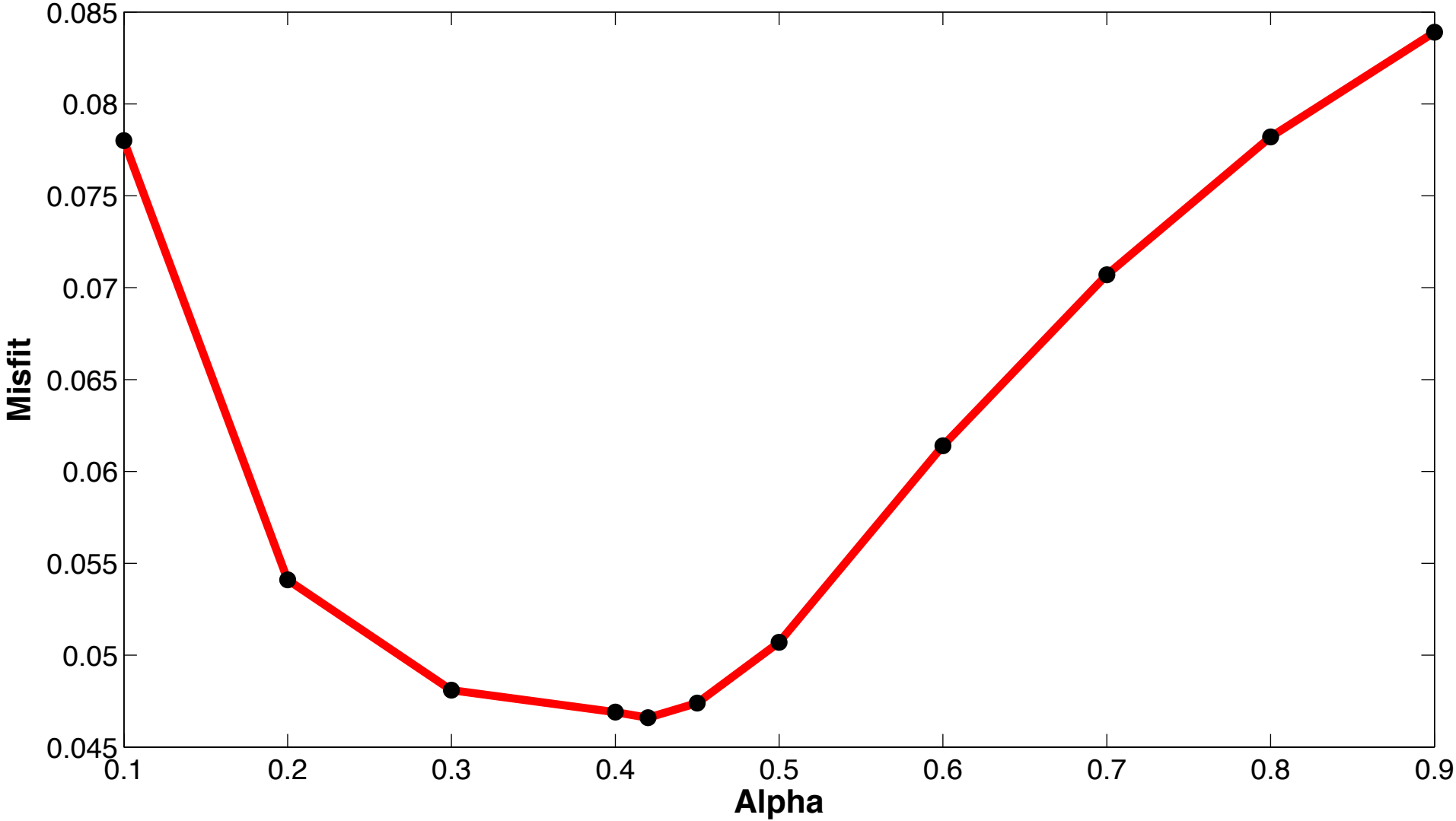
0.085
0.08
0.075
0.07
0.065
0.06
0.055
0.05
0.045
Misfit
0.1
0.2
0.3
0.4
0.5
0.6
0.7
0.8
0.9
Alpha

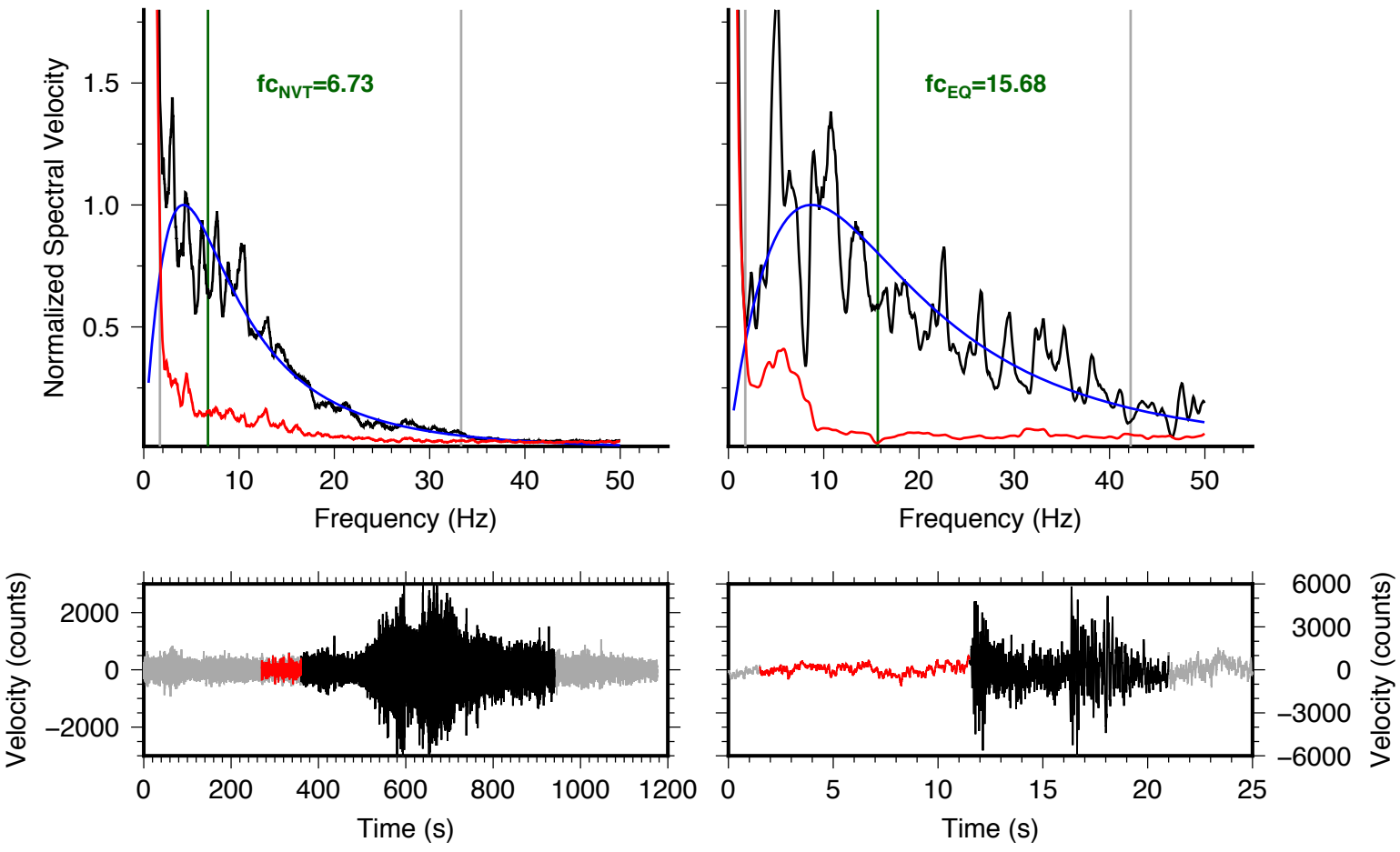
Normalized Spectral Velocity
1.5
1.0
0.5
fc$_{NVT}$=6.73
fc$_{EQ}$=15.68
0
10
20
30
40
50
Frequency (Hz)
Velocity (counts)
2000
0
−2000
6000
3000
0
−3000
−6000
0
200
400
600
800
1000
1200
Time (s)
0
5
10
15
20
25
Time (s)

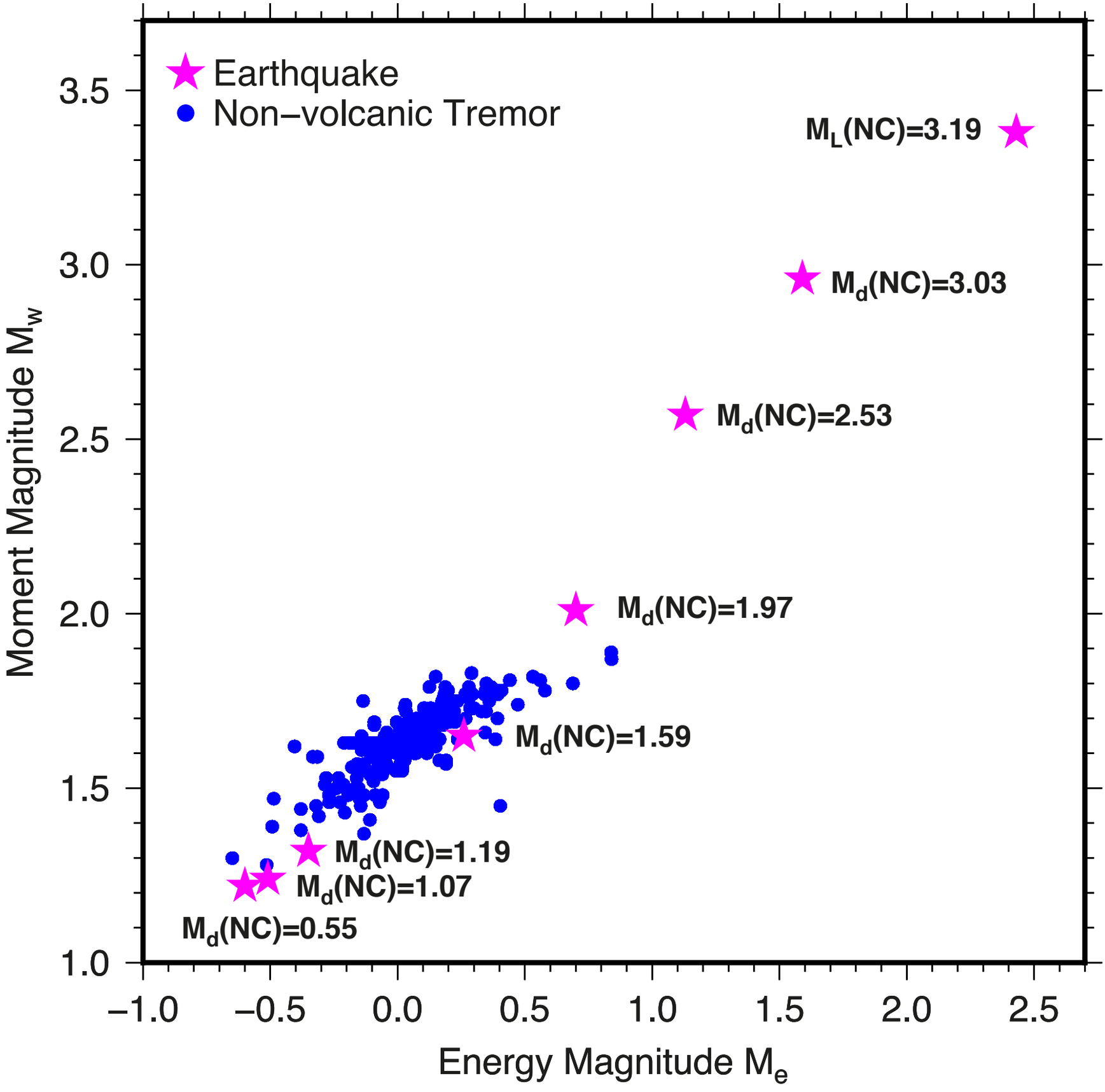
Earthquake
Non–volcanic Tremor
M_L(NC)=3.19
M_d(NC)=3.03
M_d(NC)=2.53
M_d(NC)=1.97
M_d(NC)=1.59
M_d(NC)=1.19
M_d(NC)=1.07
M_d(NC)=0.55
Moment Magnitude M_w
Energy Magnitude M_e
3.5
3.0
2.5
2.0
1.5
1.0
–1.0
–0.5
0.0
0.5
1.0
1.5
2.0
2.5

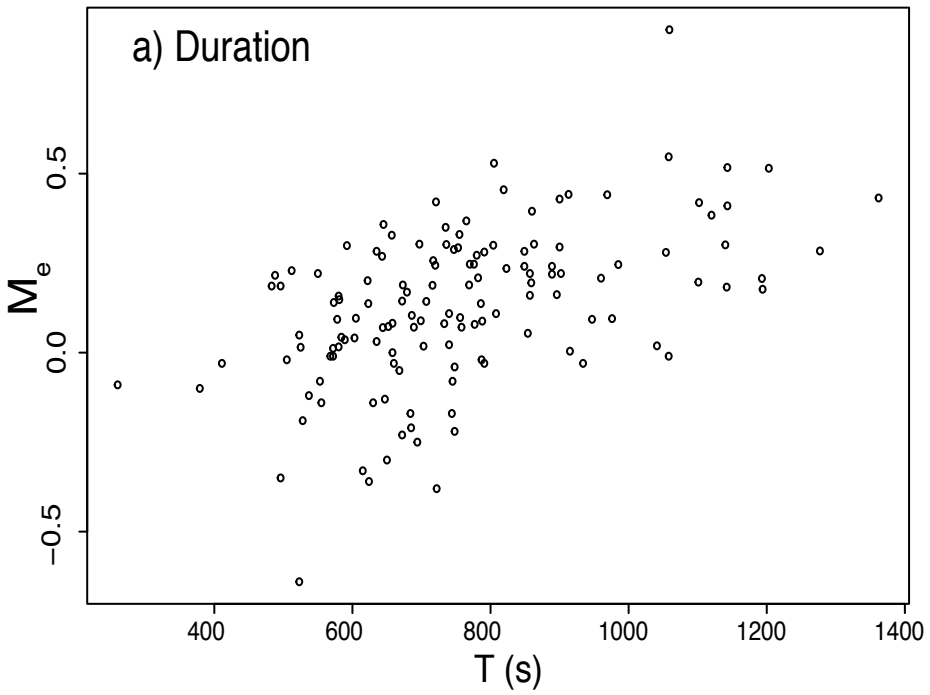
a) Duration
M_e
0.5
0.0
−0.5
400
600
800
1000
1200
1400
T (s)

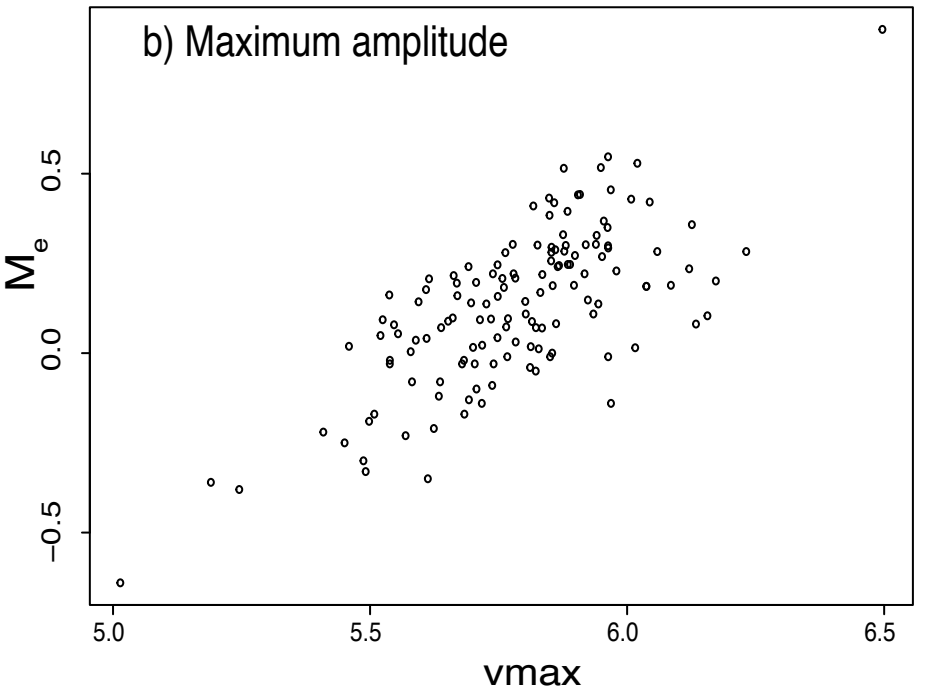
b) Maximum amplitude
M_e
0.5
0.0
−0.5
5.0
5.5
6.0
6.5
vmax

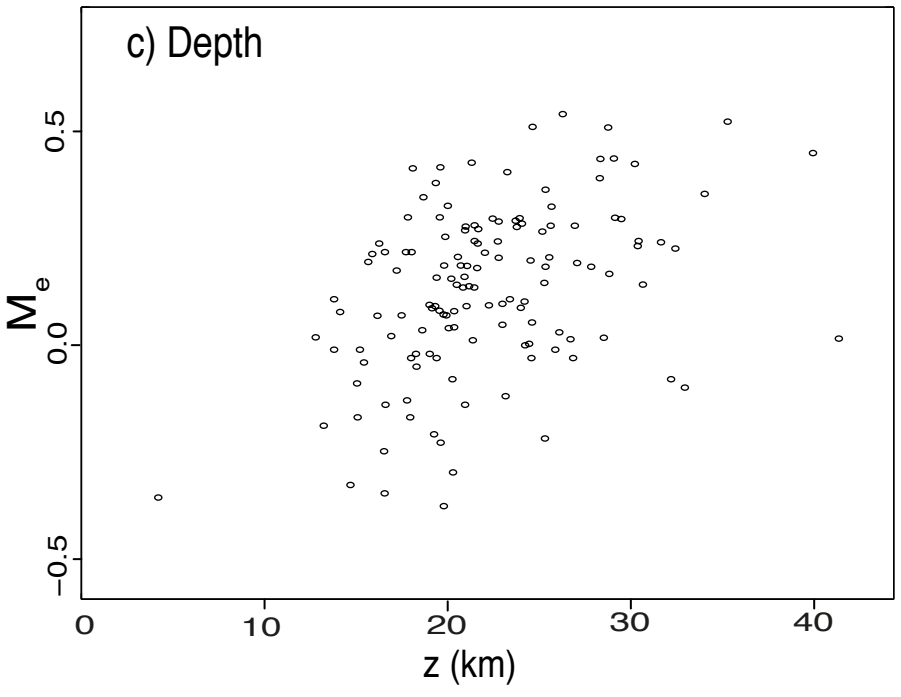
c) Depth
M_e
0.5
0.0
−0.5
0
10
20
30
40
z (km)

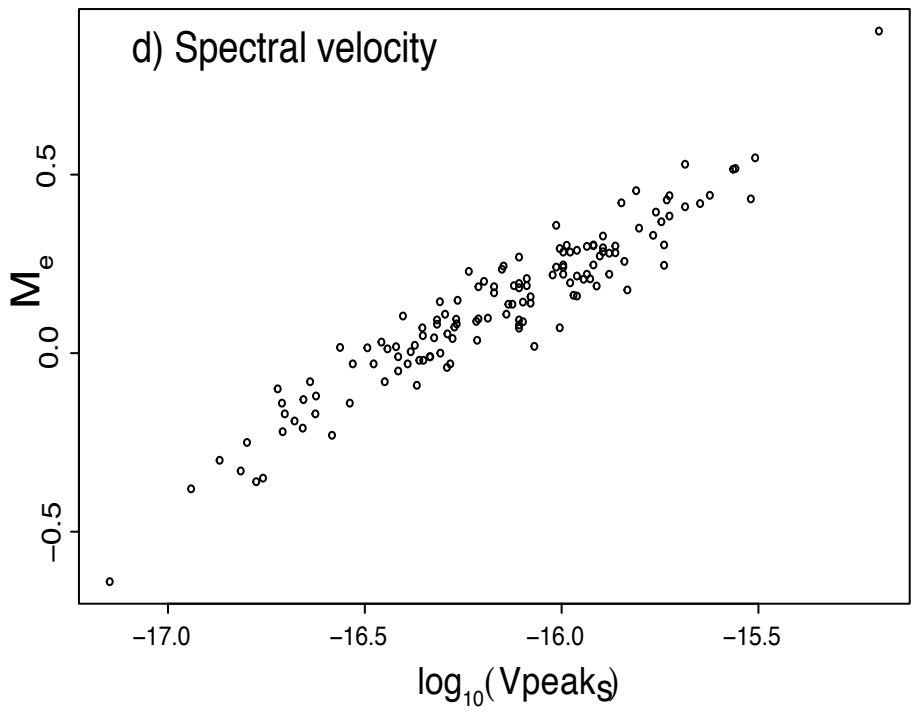
d) Spectral velocity
M_e
0.5
0.0
−0.5
−17.0
−16.5
−16.0
−15.5
$\log_{10}(\mathrm{Vpeak_S})$

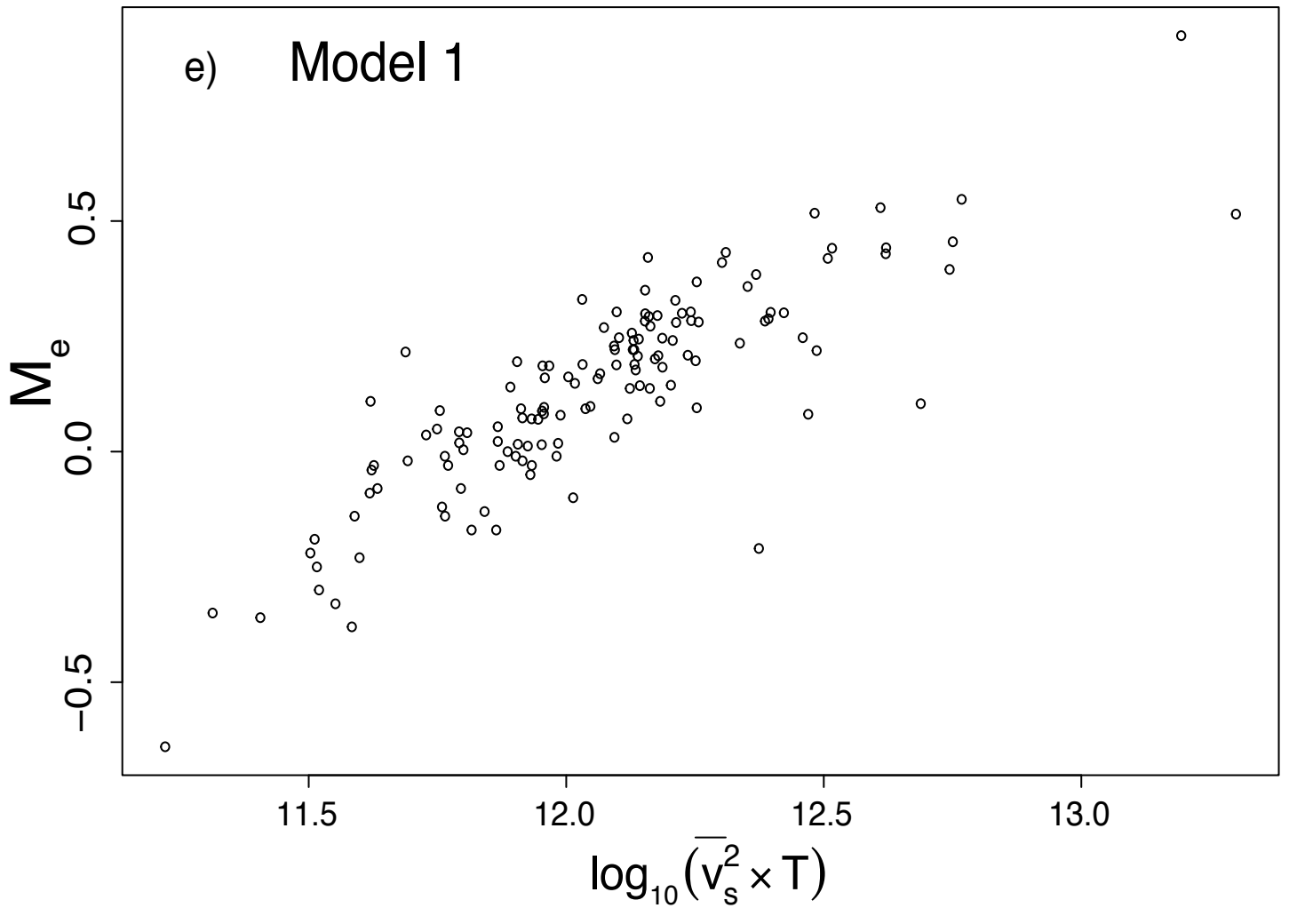
e) Model 1
M_e
0.5
0.0
−0.5
11.5
12.0
12.5
13.0
$\log_{10}(\overline{v_s^2} \times T)$

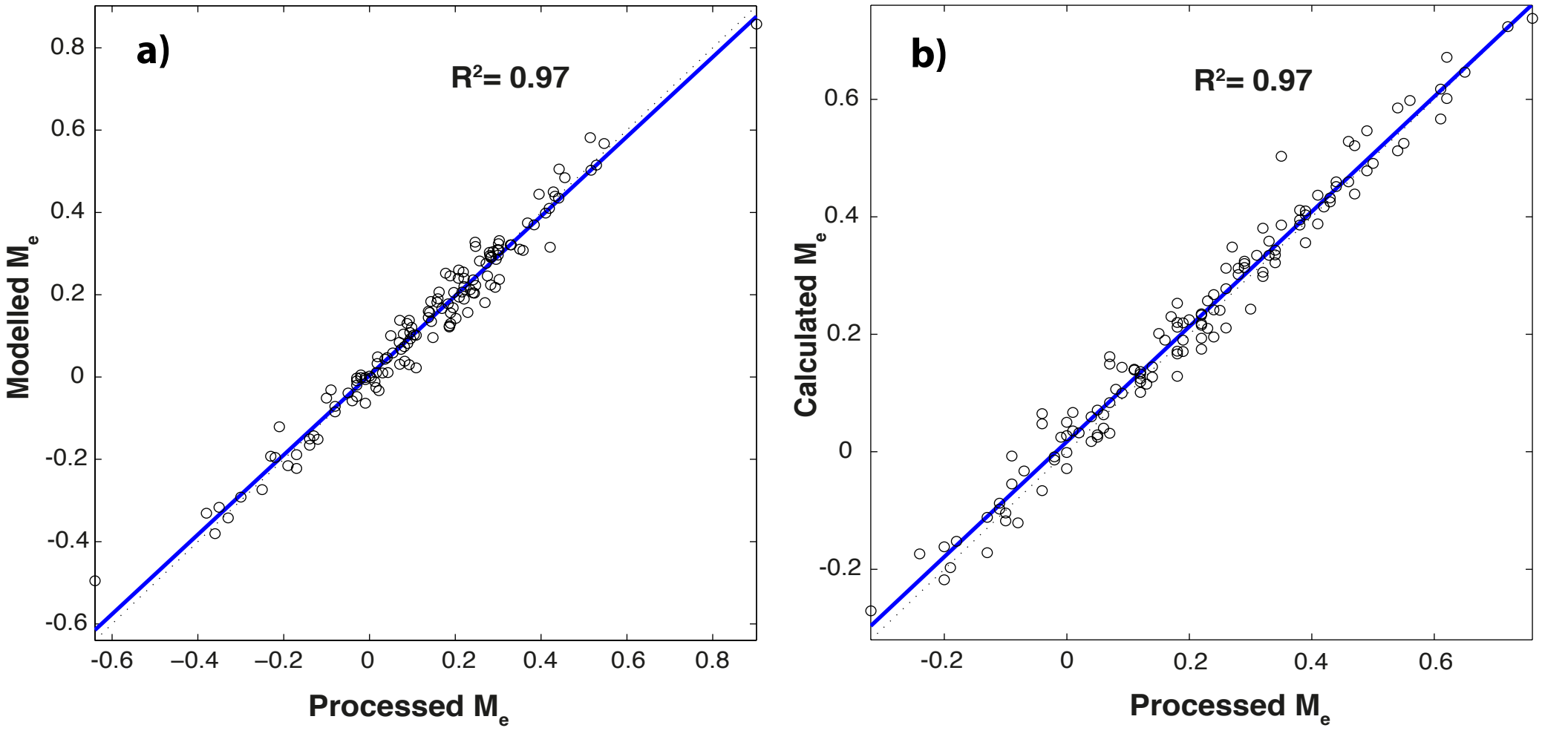
a)
R²= 0.97
Modelled M_e
Processed M_e
b)
R²= 0.97
Calculated M_e
Processed M_e

Improving plateaus

Improving plateaus

optimal attenuation (α=0.45)

over estimated attenuation (α=0.55)

3D-CC locations

At Moho depth

On fault

On single point

Spectral Velocity

Spectral Acceleration

a) b) c) d) e) f) g) h) i) j) k) l)

Frequency (Hz)

Energy Magnitude M_e

Spectral Acceleration

a)

25 Hz

49 Hz

γ >1

γ =1

γ <1

true location

Frequency (Hz)

b)

25 Hz

49 Hz

mean γ =1.18
std γ = 0.017

mean γ =0.81
std γ = 0.016

mean γ ≈ 1
std γ = 0.040

Frequency (Hz)

c)

25 Hz

49 Hz

mean γ = 1
std γ = 0.015

Frequency (Hz)

d)

Increasing location probability

cc norm
+/- 3.5km

cc norm
+/- 1km

cc norm
+/- 5km

cross corr

cross corr -5km

Moho depth

on fault plane

cloud middle

sp dd

Moho and
on fault

cross corr +5km

shuffled locations

single point locations

200

150

100

50

0

0.05

0.1

0.15

0.2

0.25

0.3

0.35

0.4

|(1-mean (γ))|+standard deviation(γ)

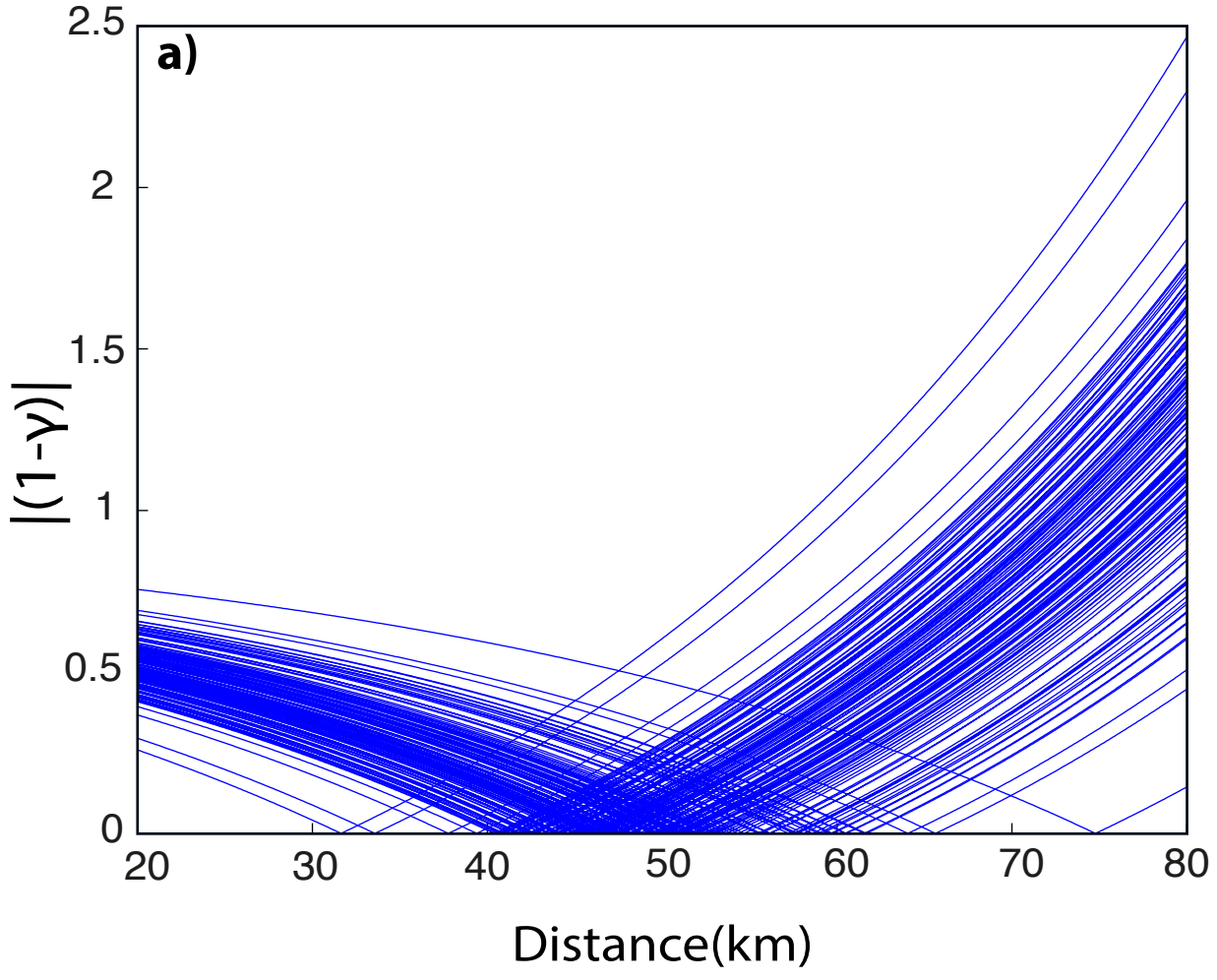
a)
|(1-γ)|
Distance(km)

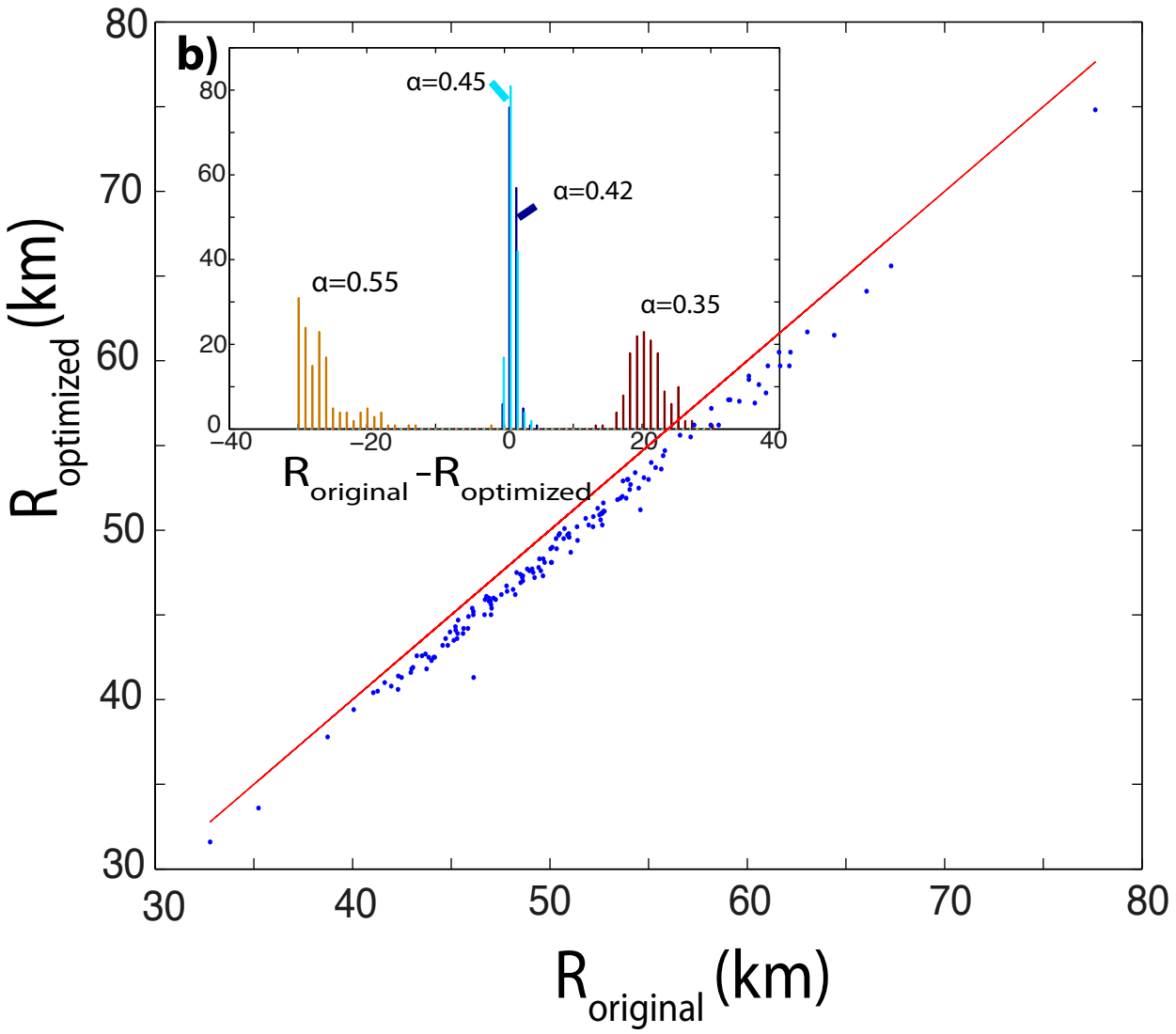
b)
α=0.45
α=0.42
α=0.55
α=0.35
R original -R optimized
R optimized (km)
R original (km)